

Hydrodynamical simulations of the Ly α forest: data comparisons

Avery Meiksin¹, Greg Bryan^{2,3}, Marie Machacek²

¹*Institute for Astronomy, University of Edinburgh, Blackford Hill, Edinburgh EH9 3HJ, UK*

²*Department of Physics, MIT, 77 Massachusetts Avenue, Cambridge, MA 02139, USA*

³*Hubble Fellow*

2 December 2024

ABSTRACT

Numerical hydrodynamical simulations are used to predict the expected absorption properties of the Ly α forest for a variety of Cold Dark Matter dominated cosmological scenarios: CHDM, OCDM, Λ CDM, SCDM, and tCDM. Synthetic spectra are constructed duplicating the resolution, signal-to-noise ratio, and wavelength coverage of several published high resolution spectra, and their statistical properties compared on the basis of the flux distribution of the spectra, the distribution of coefficients in a wavelet decomposition of the spectra, and the distributions of absorption line profile parameters. Agreement between the measured and predicted cumulative distributions is found at the few to several percent level. No single model provides an acceptable match to all the distributions; the best compromise model is a flat Λ CDM model with low normalization ($\sigma_8 = 0.8$). Larger median Doppler parameters are found in the measured spectra than predicted by those models which provide the best fits to the flux distributions. This may indicate a need to introduce additional energy injection into the intergalactic gas, as may be provided by winds from young galaxies. A larger number of narrow absorption features are found in the data than predicted by the models. Although some of these are accounted for by identified metal lines, approximately half are not at $z \lesssim 3$, suggesting either the presence of a large number of unidentified metal lines or the possibility of additional cooling of low density gas. The models require a hydrogen ionization rate at redshifts $1.7 < z < 3.8$ within a factor of 2–3 of that predicted for QSOs alone as the sources of the UV photoionization background. A principal uncertainty in comparing the models with the observations is the setting of the continuum level of the QSOs.

Key words: hydrodynamics – methods: numerical – intergalactic medium – quasars: absorption lines – cosmology: theory – large-scale structure of Universe

1 INTRODUCTION

The successful reproduction of the observed statistical properties of the Ly α forest by numerical simulations in the context of various cold dark matter (CDM) dominated cosmologies suggests that the gravitational instability scenario provides a broadly accurate description of the development and evolution of the structure of the Intergalactic Medium (IGM) (Cen et al. 1994; Zhang, Anninos, & Norman 1995; Hernquist et al. 1996; Zhang et al. 1997; Bond & Wadley 1997; Theuns, Leonard & Efstathiou 1998). The simulations show that nearly the entire IGM fragments into filaments, sheets, and fluctuations in underdense minivoids, all of which give rise to the absorption lines comprising the Ly α forest detected in the spectra of Quasi-Stellar Objects (QSOs) (Cen et al. 1994; Zhang et al. 1998). By analysing

synthetic spectra drawn from the simulations, it has been demonstrated that the measured flux distributions, neutral hydrogen column density distributions, and the evolution in the number of absorption lines per unit redshift are reasonably well accounted for by the complex web of interconnecting structures found in the simulations. An outstanding difficulty is the somewhat poorer agreement in the distributions of line-widths, or Doppler parameters, though this may be a reflection of the choice of cosmological parameters, particularly the baryon fraction, or the uncertainty in the reionization scenario of the gas.

The comparisons made to date have largely been based on idealised realisations of synthetic spectra, without direct reference to the wavelength coverage, resolution and signal-to-noise ratios of the measured spectra. A detailed comparison with the composite flux distribution in a set of

QSO spectra measured by the Keck HIRES was made by Rauch et al. (1997) for two cosmological models, Λ CDM and SCDM, but this has not been extended to a broader range of models. No group has exhausted the information available from Voigt profile absorption line fitting to the synthetic and observed spectra.

The structure of the Ly α forest is intermediate in complexity between that of the Cosmic Microwave Background (CMB) and the large-scale distribution of galaxies. It may be reasonably hoped that the physics of gravitational instability and hydrodynamics alone, once a model for the reionization of the IGM is assumed, is adequate for describing the measurements of the Ly α forest. This is similar to the situation for the CMB, where it appears linear instability theory involving only the physics of gravity and hydrodynamics is adequate for providing an accurate description of the fluctuations over the range of measured scales, but is in contrast to the clustering of galaxies, which appears increasingly complex as it is studied in greater detail, and will likely inevitably require an understanding of the formation and evolution of galaxies, their stars, and the associated feedback mechanisms before a complete description of the large-scale spatial distribution of galaxies is derived. From the perspective of the underlying physics, the Ly α forest represents a bridge between the relatively straightforward mechanisms believed responsible for the formation of the CMB fluctuations (given an input cosmological model and linear power spectrum), and the complex physical processes involved in galaxy formation. For this reason, the Ly α forest offers a unique forum for testing models of structure formation.

The objective of this paper is to make a detailed comparison of the predictions of numerical models of the Ly α forest with the measured properties as revealed directly by QSO spectra. A principal theme is to determine how closely the simulations match the statistics of the Ly α forest extracted from the measured spectra, and to determine the limitations involved, both observational and theoretical. As a pilot program in this investigation, a suite of simulations for a variety of cosmological models is used to construct synthetic spectra designed to match the resolution and signal-to-noise ratios of a set of measured spectra reported in the literature. Both the synthesized and measured spectra are analysed using identical software to minimize any differences due to the arbitrary nature of the algorithms. In this way, we are able to determine how sensitive the statistics of the absorption features are to the properties of the spectra, including data-reduction systematics, especially the uncertainty in the continuum-fitting. Ultimately we would like to know whether or not the data and the simulations are of adequate accuracy to distinguish between differing cosmological models and reionization scenarios. If so, the simulations could provide an independent tool both to test models for structure formation as well as to probe the physical state of the gas and the energetic processes that accompanied the formation of early sources of photoionization, whether QSOs, galaxies, or smaller stellar systems.

The paper is organised as follows. In the next section we describe the methods used to compare the simulation results with the measured spectra. In §III, the analysis results for 7 QSO spectra are presented. A discussion of the results follows in §IV. Our conclusions are summarised in §V. Various

tests of the analysis procedures and absorption line fitting algorithms are discussed in the two appendices.

2 ANALYSIS METHODS

2.1 Model spectra

The models used in the paper are described in detail in Machacek et al. (2000) (M00) and summarised in Table 1. All the models considered are in the context of CDM dominated cosmologies. The following five models were simulated using Kronos, a combined PM + PPM gravity-hydrodynamics code: a standard critical-density flat CDM model (SCDM), a flat CDM model with a nonvanishing cosmological constant (Λ CDM), an open CDM model (OCDM), the standard CDM model but with the power spectrum of the density perturbations tilted (tCDM) to match the normalization on large scales as determined from the COBE measurements of the Cosmic Microwave Background (Bunn & White 1997), and a flat critical-density mixed dark matter model with a hot component added to the CDM (CHDM). An additional Λ CDM model was also computed similar to the first, but with a lower normalization of the power spectrum, a higher baryon density, and the rate of He II heating by QSO sources increased by a factor of 1.8 to mimic the sudden onset of He II photoionization (Bryan & Machacek 2000) before radiative recombinations to He II have had time to reduce the heating rate (Meiksin 1994). The initial data for all models except CHDM and the higher baryon density Λ CDM model were generated using COSMICS (Bertschinger 1995) with the BBKS transfer function (Bardeen et al. 1986) to compute the starting redshifts and the unconstrained initial particle positions and velocity perturbations appropriate for each model. For the CHDM model we used CMBFAST (Seljak & Zaldarriaga 1996) to generate the initial conditions. For the higher baryon density Λ CDM model, the power spectrum was based on the analytic fits of Eisenstein & Hu (1999).

We use the synthetic spectra described in M00. We construct the spectra with the pixelizations given in Table 2. We mimic the spectral resolution by smoothing the spectra with a gaussian of the indicated widths.

In order to construct spectra with the identical wavelength coverage as the observed spectra, the simulation results from a broad range in redshifts must be used. Since the simulation results are saved at only integral redshift values between $z = 1$ and $z = 5$ (except for the higher baryon density Λ CDM model, for which the data are saved more frequently), it is necessary to interpolate between redshifts. (We do not use the $z = 1$ results since the fundamental mode across the simulation volume has grown too large by this time to be certain of the reliability of the results.) To assist in the interpolation, we take advantage of the redshift scaling relations of the gas properties found by M00. Because the gas is in photoionisation equilibrium, we may expect the optical depth at any given wavelength to scale like $\tau(\lambda) \propto n^2 \alpha_A(T) / [\Gamma(z) H(z)]$, where n is the gas density, $\alpha_A(T)$ is the (Case A) radiative recombination coefficient at gas temperature T , $H(z)$ is the Hubble constant at redshift z , and $\Gamma(z)$ is the incident rate of ionising photons per neutral atom. It was demonstrated by

Zhang et al. (1998) that the morphologies and overdensities of the overdense structures evolve only slowly in the comoving frame. Since additionally T was found to scale like a power of the gas density, and $\alpha_A(T) \propto T^{-0.7}$ (approximately), we may expect the combination $n^2 \alpha_A(T)$ to scale like a power of the mean gas density $\bar{n}(z)$, which itself scales as $(1+z)^3$. Accordingly, we scale the optical depths according to $\tau(z) \propto (1+z)^\alpha / [\Gamma(z)H(z)]$. For any particular cosmological model, we determine α between two redshifts z_1 and z_2 by finding the value which best predicts the mean optical depth, defined by $\bar{\tau}_\alpha \equiv -\log\langle\exp(-\tau)\rangle$ averaged over the spectra, at $z = z_2$ using the spectra at $z = z_1$. (In principle, a different value for α may be found by reversing the roles of z_1 and z_2 . We checked this and found in all cases the same value for α was derived.) The values found are provided in Tables 3 and 4. We allow for an overall rescaling of the radiation field by multiplying the optical depths by a scale factor s . (The factor s could also be interpreted as a rescaling of the baryon density, although this would entail a change in the gas temperature, which we do not allow for.) The UV background radiation field adopted in the simulations evolves according to the model of Haardt & Madau (1996) predicted for QSOs as the sources of the radiation, and assuming an intrinsic QSO spectral index $\alpha_Q = 1.5$. We additionally accommodate an alternative evolution in the radiation field by allowing for a further evolution factor $(1+z)^p$ for $\Gamma(z)$. Thus we predict τ at any given wavelength λ at redshift z based on the value at redshift z_1 at wavelength $\lambda(1+z)/(1+z_1)$ according to

$$\tau(z) = s\tau(z_1) \left(\frac{1+z}{1+z_1}\right)^\alpha \left(\frac{1+z}{1+z_{\text{ref}}}\right)^p \frac{\Gamma(z_1)H(z_1)}{\Gamma(z)H(z)}, \quad (1)$$

where z_{ref} is a reference redshift introduced for $p \neq 0$. The values for s , p , and z_{ref} adopted for different cosmologies required to match the measured spectra are provided below.

The interpolation to intermediate redshifts to cover the wavelength range of a particular measured spectrum is accomplished by generating spectral segments from the simulations, each a fixed redshift interval $\Delta z = 0.1$ in length, scaling the optical depth in each segment according to equation 1, and then effectively piecing the segments together to match the wavelength range of the measured spectrum. In order to interpolate between two data dumps at redshifts z_1 and z_2 , we compute the distribution functions $f(x; z, z_d)$ for any given statistic x within a redshift interval $(z, z + \Delta z)$ by first extrapolating the optical depths from a data dump at z_d to z , and then computing the final distribution function for a redshift interval $z_b < z < z_a$ according to

$$f(x) = \sum_i \Delta z [w_{2,i} f(x; z_i, z_1) + w_{1,i} f(x; z_i, z_2)], \quad (2)$$

using the linear weights $w_{j,i} = |(z_i - z_j)/(z_2 - z_1)|$, and incrementing z_i from z_b to z_a . We find this procedure recovers the distribution functions at intermediate redshifts to very high accuracy, as is shown in Appendix A.

In all cases, the wavelength coverage $z_b < z < z_a$ corresponds to a range between Ly α and Ly β in the QSO rest-frame. In practice the ranges are usually shortened to a smaller interval, depending on the wavelength coverage of the spectrum and to avoid the local photoionizing influence of the QSO (the proximity effect).

A major uncertainty in comparing with the measured

spectra is the setting of the continuum level. Normally peak flux points are used to set the level of the continuum in the Ly α forest region of the spectrum. In regions where the flux never recovers to the true continuum, however, this procedure will result in an underestimate of the continuum level. Without an automated procedure for inferring the continuum within the forest, it is difficult to gauge the effect of the uncertainty in the continuum level. We find that making no correction to the continuum frequently results in a mismatch in the flux distribution for flux values near unity (in units of the continuum). We model errors in the continuum level by allowing for a shift in its overall value according to:

$$F_i = \frac{F_i^{(0)}}{1 - \omega}, \quad (3)$$

where $F_i^{(0)}$ is the flux predicted by the numerical model at pixel i , and F_i is a corrected flux allowing for a downward shift in the continuum level by the fractional amount ω , applied uniformly across the spectrum. This is a crude approximation to the actual errors likely to occur. We adopt it for its simplicity in order to assess the impact of possible continuum errors. For a more accurate comparison, it would be necessary to re-analyse the raw data and offset the simulation spectra at each pixel following a procedure consistent with that of the observers.

The fitting of absorption lines to the spectra requires a noise value for each pixel. We adopt two methods for introducing noise into the simulated spectra. In the first procedure, we create a noise array from the 1σ noise levels in the observed spectra, averaging the noise over redshift intervals of width $\Delta z = 0.1$. We then generate noise from the array, assuming the noise to be gaussian distributed. This allows us to model a varying signal-to-noise ratio across a spectrum. A refinement of this method is to generate a noise matrix depending on redshift and flux value, allowing for a correlation between flux and noise. In practice very similar results are obtained for the statistical properties of the simulated spectra, as shown in Appendix A.

2.2 Analysis tools

There are several statistics that may be used as a basis of comparison between the models of the Ly α forest and the observed spectra. The most fundamental is simply the distribution of flux per pixel. Additional constraints are provided by the fluctuations in the spectra, which are related both to the underlying baryon density fluctuations and to the thermal and velocity widths of the associated absorption lines. We quantify the fluctuations in two ways. The scales of fluctuation of the spectral features may be directly characterised using wavelets, which quantify the changes in a given spectrum on being smoothed from one velocity resolution to another (Meiksin 2000). A multiscale analysis based on the Daubechies wavelets effectively performs a smoothing of the spectrum over successive doublings of the pixel width, weighted such that the spectra are decomposed into orthogonal components corresponding to different velocity scales. We use the Daubechies wavelet of order 20.

The most traditional method for analysing the light fluctuations in a spectrum is to decompose the spectrum into a set of Voigt line profiles. We utilise AutoVP (Davé

et al. 1997) to perform this analysis. In order to determine the sensitivity of the resulting distributions of absorption line parameters to the line analysis method, we have also developed a separate algorithm called SPECFIT. Rather than searching for absorption maxima, and adjusting the number of lines required for a good fit, as does AutoVP, SPECFIT first splits the spectra into segments bordered by flux values above that corresponding to a minimum optical depth threshold τ_{\min} , and then searches for inflection points in noise-filtered representations of the data in each segment in order to identify the locations of candidate absorption lines. The candidate lines are then fit to the original spectrum. While less sophisticated than AutoVP, SPECFIT operates a factor of 50-100 faster with a comparable level of success in the fits, except that it sometimes misses the weakest optically thin features ($\tau < \tau_{\min}$). The two methods are compared in Appendix B.

2.3 Data

We compare the simulation results with 6 Keck HIRES spectra and 1 VLT UVES spectrum that have been published in the literature. The quasars, the redshift ranges used in the comparison, the pixel resolutions of the spectra, and the spectral resolutions, are summarised in Table 2. All the spectra were normalized to a unit continuum level by the observers.

3 RESULTS

In this section, we compare the distributions of flux per pixel, wavelet coefficients, and absorption line parameters for each of the QSO spectra in Table 2. The amplitudes of the distributions found in the models cannot be used as a basis for comparison since the optical depths may be arbitrarily re-scaled for any individual model by the ionization bias factor $b_{\text{ion}} \propto \Omega_b^{1.6}/\Gamma$.^{*} It is important to normalize all the models consistently with any given measured QSO spectrum before comparing the shapes of any of the distributions with those measured. This may be done in a variety of ways. We do so by matching the mean H I optical depth $\bar{\tau}_\alpha$ in each simulation to the measured intergalactic H I optical depth over the comparison redshift range. Since the resulting model flux distributions will often mismatch the observed distributions for flux values near unity, we will also allow for a constant offset as given by equation 3, while keeping the value of $\bar{\tau}_\alpha$ fixed at the observed value. In some instances it is also found necessary to introduce additional evolution in the UV radiation background to that adopted in the simulations.

^{*} Because of a weak dependence on the gas temperature, the scaling depends somewhat more weakly than Ω_b^2/Γ . The results in Zhang et al. (1998) give $T \simeq 8000(\rho_b/\bar{\rho}_b)^{1/2}$ K for systems with $12.5 < \log N_{\text{HI}} < 14.5$. Combining with the temperature dependence of the radiative recombination coefficient, $\alpha_A \propto T^{-0.7}$, gives $b_{\text{ion}} \propto \Omega_b^{1.6}/\Gamma$.

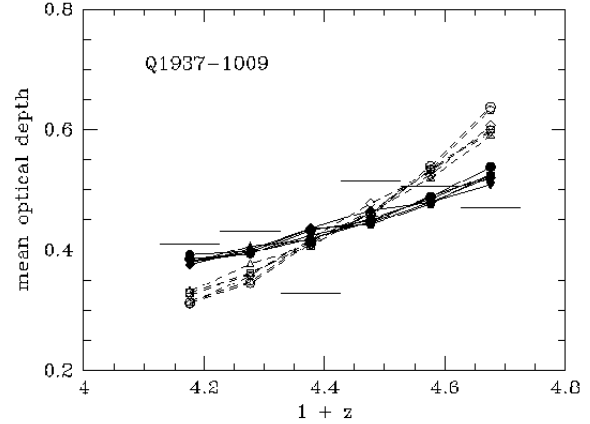


Figure 1. Redshift dependence of mean optical depth $\bar{\tau}_\alpha$ for Q1937-1009. The open symbols show the values for $\bar{\tau}_\alpha$ found in the simulations based on the evolution of the UV radiation background as determined from QSO sources by Haardt & Madau (1996). The filled symbols show the values for $\bar{\tau}_\alpha$ after allowing for an alternative redshift dependence of the UV radiation background. The symbols are: CHDM (circles), Λ CDM_L (squares), Λ CDM_H (diamonds), OCDM (triangles), SCDM (inverted triangles), tCDM (pentagons).

3.1 Q1937-1009

3.1.1 Flux distribution

We investigate Q1937-1009 (Burles & Tytler 1997) most thoroughly in order to assess the magnitude of some of the possible systematics in our analyses. Over the redshift range $3.126 < z < 3.726$, the mean optical depth in the measured spectrum is $\bar{\tau}_\alpha = 0.44$. The mean optical depths in redshift intervals $\Delta z = 0.1$ wide are shown in Figure 1, along with estimates from each of the models. (The noise array adopted in the simulated spectra is independent of pixel flux here. It is shown in Appendix A that introducing a flux-dependent noise dispersion has little effect on the statistics. For the remaining QSO spectra analysed in this paper, the flux-dependent noise model is adopted.) The optical depth per pixel has been rescaled according to equation 1 for each model, using the parameter values given in Table 3. The measured values of $\bar{\tau}_\alpha$ are nearly flat with redshift. Formally they are well fit by $\bar{\tau}_\alpha = a(1+z)^b$, with $a = 0.022^{+0.044}_{-0.015}$ and $b = 2.0 \pm 0.74$, where the standard deviation of the measured values of $\bar{\tau}_\alpha$ is adopted as a measurement error for each value. By contrast, the models predict a near doubling

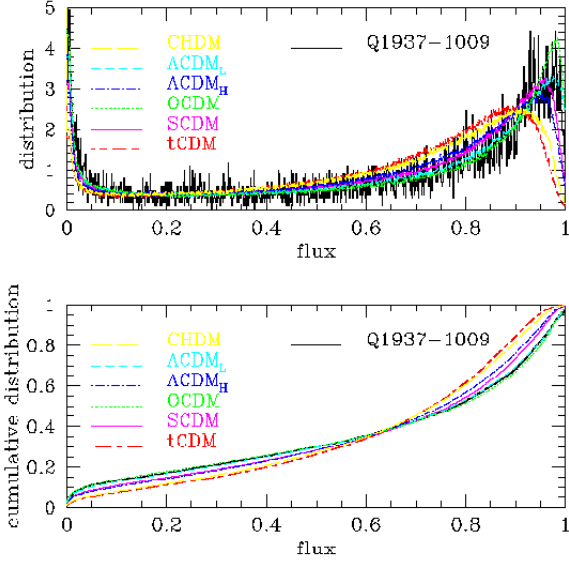


Figure 2. Comparison between measured flux distribution of Q1937–1009 and the model predictions. Particularly good agreement is found for the OCDM and Λ CDM_L models.

of the mean optical depth over the same redshift interval, corresponding to $b = 6$, significantly steeper than measured. It is evident that an alternative evolution rate to that of the simulations is required to match the redshift dependence of the mean optical depths. To match the observed evolution, we adopt the additional rate exponents p for $z_{\text{ref}} = 3$ (cf equation 1) as given in Table 3. The resulting distributions of $\bar{\tau}_\alpha$ for the various models are shown in Figure 1.

The distributions of flux per pixel for the various models are compared with the observed distribution in Figure 2. (Flux values exceeding unity are due to noise fluctuations.) The agreement is generally good, particularly for the OCDM and Λ CDM_L models. The models all show some disagreement at flux values near unity, and for this reason they may all be formally rejected by the KS test. The best agreement is for OCDM, with a maximum difference (in absolute value) between the predicted and measured cumulative distributions of $d_{\text{KS}} = 0.024$, corresponding to a formal acceptance probability of $P_{\text{KS}} = 10^{-5}$. The Λ CDM_L model gives $d_{\text{KS}} = 0.040$ and $P_{\text{KS}} = 2 \times 10^{-14}$.

Allowing for the possibility that the continuum level in the observed spectrum was set slightly low, resulting in overestimates of the normalized flux, we increase the flux per pixel according to equation 3, choosing values for s and ω that simultaneously preserve $\bar{\tau}_\alpha = 0.44$ and match the measured flux distribution at flux values near unity. The resulting flux distributions are shown in Figure 3, using the

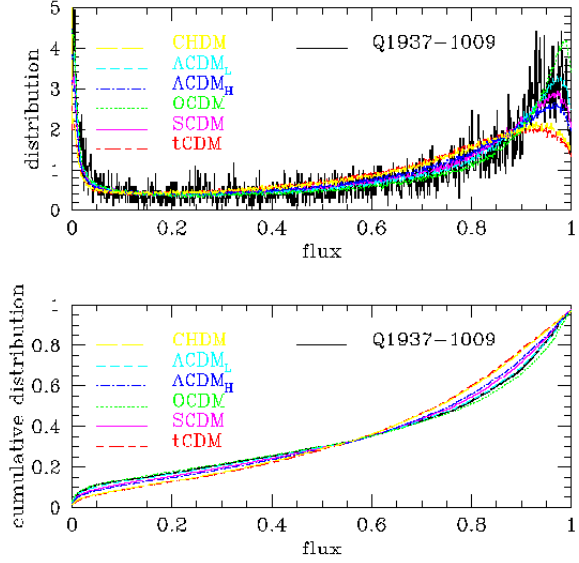


Figure 3. Comparison between measured flux distribution of Q1937–1009 and the model predictions. A continuum offset was applied to each model to enforce matching the cumulative distributions at flux values near unity. The distributions tighten compared with Figure 2. The Λ CDM_L model is now preferred over OCDM.

values for s and ω in Table 3. The agreement in the cumulative distributions is now tightened, with the Λ CDM_L model agreeing best with the observed distribution. For the Λ CDM_L model, $d_{\text{KS}} = 0.013$, corresponding to a formal acceptance probability by the KS test of $P_{\text{KS}} = 0.059$. By comparison, the next best model is OCDM, with $d_{\text{KS}} = 0.038$, and is strongly rejected by the KS test, with an acceptance probability of $P_{\text{KS}} = 3 \times 10^{-13}$.

We note that the KS test is based on the probability distribution for $N^{1/2}d_{\text{KS}}$, where N is the number of independent measurements in the sample. We find that the probability distribution for this quantity based on the simulated spectra is broader than the theoretical distribution. Because of the limited number of lines-of-sight drawn from the simulation volume, it is not possible to attach meaningful probabilities to large values of d_{KS} directly from the simulations. The values of P_{KS} are only an indication of the relative levels of success of the models. We discuss the distribution of d_{KS} further in Appendix A.

3.1.2 Wavelet coefficient distributions

The distribution of wavelet coefficients is shown in Figure 4 with no continuum offset, and Figure 5 with the offsets in Table 3 applied. All the models show some disagreement with

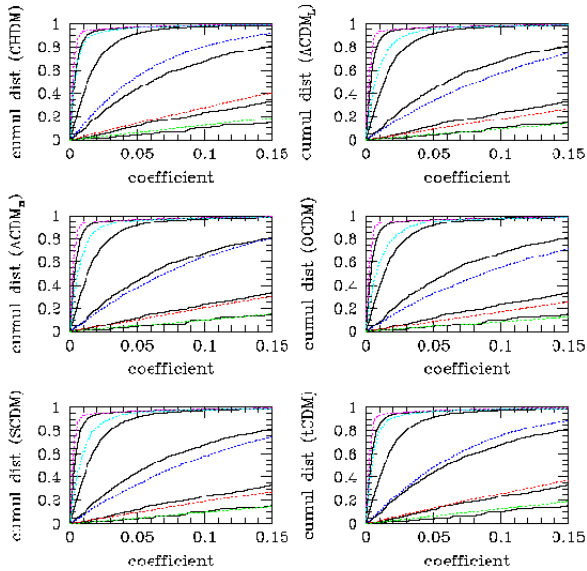


Figure 4. Comparison between the measured wavelet coefficient cumulative distributions of Q1937–1009 (solid lines) and the model predictions (dotted lines). The curves from left to right correspond to the approximate velocity scales $4\text{--}8\text{ km s}^{-1}$, $8\text{--}17\text{ km s}^{-1}$, $17\text{--}34\text{ km s}^{-1}$, $34\text{--}68\text{ km s}^{-1}$, $68\text{--}136\text{ km s}^{-1}$. The best match for the velocity scales $17\text{--}34\text{ km s}^{-1}$, corresponding to the median velocity width of the absorption features, is found for the ΛCDM_H and tCDM models. All the models underpredict the amount of velocity structure on the scales $8\text{--}17\text{ km s}^{-1}$.

the measured distribution at the smallest velocity scales $\sim 4\text{--}8\text{ km s}^{-1}$. A possible explanation is that the pixelization and smoothing (to approximate the spectral resolution) used to simulate the spectrum of Q1937–1009 are inadequate. An alternative explanation is that the simulations themselves are not able accurately to compute fluctuations on such small scales. Indeed, for an expansion velocity difference across the simulation box at $z = 3.5$ of $\sim 1000\text{ km s}^{-1}$ and 256 grid zones along a side, the characteristic velocity resolution is $\sim 4\text{ km s}^{-1}$, so that it may be difficult to simulate fluctuations in the spectra on this scale. A discrepancy, however, is again found on the larger scale of $8\text{--}17\text{ km s}^{-1}$, with the observed spectrum showing a greater amount of velocity structure (as shown by the larger values of the coefficients). In this case the discrepancy may be real. The same pixel resolution and smoothing applied here were also applied to the Monte Carlo realizations of the Ly α forest measured in Q1937–1009 by Meiksin (2000), where excellent agreement was found on the scales $8\text{--}17\text{ km s}^{-1}$, demonstrating the adequacy of the modelling of the spectra on these scales. The discrepancy between the models and data found

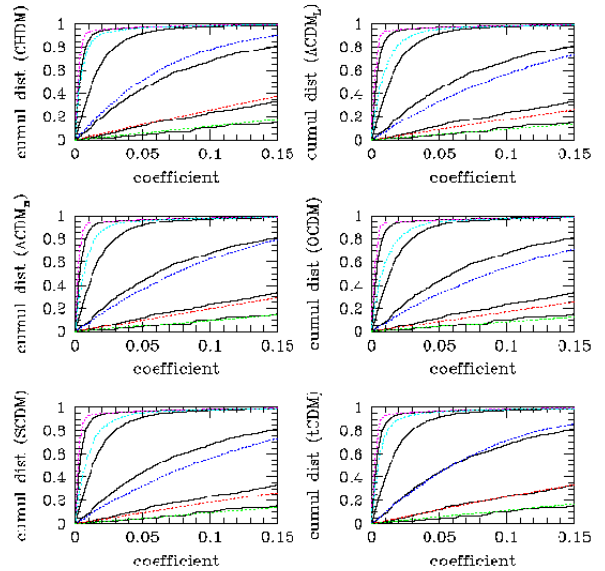


Figure 5. Comparison between the measured wavelet coefficient cumulative distributions of Q1937–1009 (solid curves) and the model predictions (dotted curves), allowing for continuum offset corrections. The curves from left to right correspond to the same sequence as in Figure 4. The offsets have little effect on the distributions, with a marginal improvement in the agreement between the tCDM predictions and the measured distributions.

here suggests a greater number of absorption features in the data on these scales.

The agreement between the models and the data improves at larger velocity scales, with particularly good agreement obtained by the ΛCDM_H and tCDM models on the scales $17\text{--}34\text{ km s}^{-1}$, typical velocity widths for the absorption features (see below). The agreement with tCDM improves when continuum offsets are included. This is in contrast to the flux distributions, for which the best agreement was found for the OCDM and ΛCDM_L models. These latter models show too great an amount of velocity structure on scales of $17\text{--}34\text{ km s}^{-1}$, while the CHDM model shows too little. The agreement continues to improve for all models at larger velocity scales.

3.1.3 Absorption line parameter distributions

The H I column density and Doppler parameter distributions resulting from fitting absorption lines to the spectra are shown in Figure 6. The spectra were fit using AutoVP. For each model, effectively 50 separate spectra were constructed from the simulation box corresponding to the identical spectral range analysed in Q1937–1009. The profile analysis is computationally expensive. For the range of column densi-

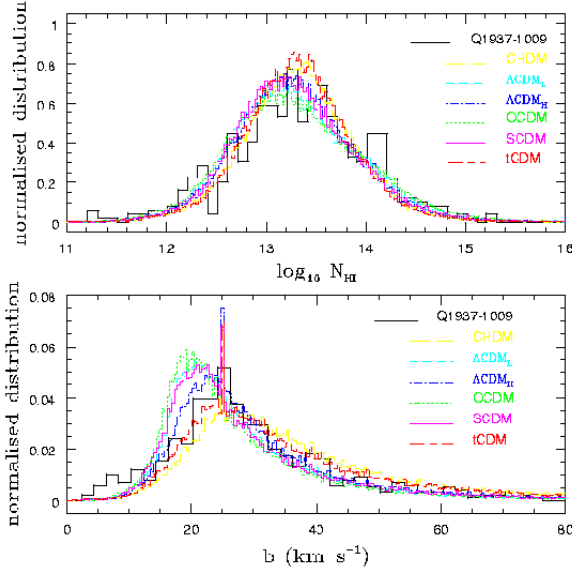


Figure 6. Comparison between the measured absorption line parameter distributions of Q1937–1009 and the model predictions. While good agreement is generally found for the N_{HI} distributions, the measured b -distribution is generally skewed toward higher b -values than most of the model predictions. The sharp peak in the simulation results at $b = 25 \text{ km s}^{-1}$ is an artefact of AutoVP.

ties of interest, it is adequate to fit the spectra using Doppler profiles rather than full Voigt profiles. We find there is little difference in the resulting distributions, while a factor of two is saved in the computing time. Typically 2.5×10^4 features in total were found for each model, requiring an analysis time of $\sim 1 - 2 \times 10^5$ cpu seconds on a Compaq XP900 with a 1GHz processor.

The agreement in the distribution of N_{HI} between the data and all the models is reasonably good, with the prediction of OCDM providing the best match. The predicted b -distributions for ΛCDM_L , OCDM and SCDM, however, generally peak at lower values than does the measured distribution. The best agreement is found for ΛCDM_H , as in the wavelet analysis.

There is an excess number of low b -parameter systems in the range $6\text{--}12 \text{ km s}^{-1}$ compared with the simulations. The discrepancy corresponds to the greater amount of velocity structure on these scales found in the wavelet analysis, demonstrating that the features are not artefacts of the absorption line analysis procedure. It is likely that the narrow features in the data are metal lines. We return to this possibility below in connection with Q1946+7658.

The cumulative distributions are shown in Figure 7. The measured N_{HI} distribution is best matched by the OCDM

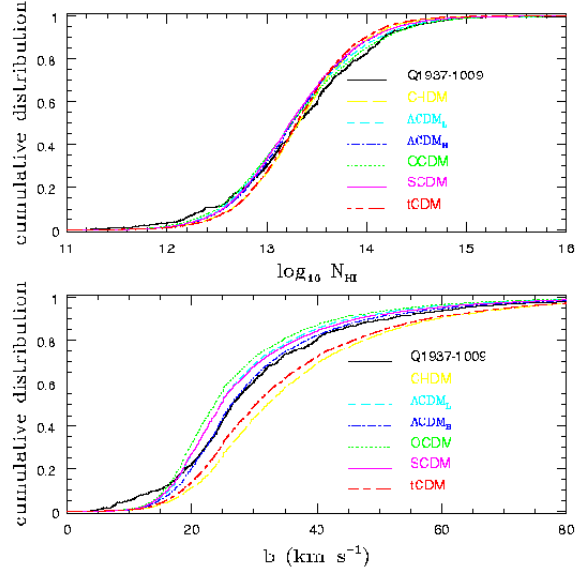


Figure 7. Comparison between the measured absorption line parameter cumulative distributions of Q1937–1009 and the model predictions using AutoVP. The OCDM and ΛCDM_L models agree best with the measured N_{HI} distribution. The ΛCDM_H model agrees best with the measured b -distribution.

and ΛCDM_L models. The maximum differences in the measured and predicted cumulative distributions for the OCDM and ΛCDM_L models are, respectively, $d_{\text{KS}} = 0.059$ and 0.067 , with the associated formal acceptance probabilities of $P_{\text{KS}} = 0.062$ and 0.024 . The ΛCDM_H model best reproduces the measured b -distribution, with $d_{\text{KS}} = 0.060$ and $P_{\text{KS}} = 0.058$. The predictions of all other models are strongly rejected by the KS test. In particular, the OCDM model, which provides the best match to the flux distribution (assuming no continuum offset) and to the N_{HI} distribution, predicts too small a median Doppler parameter. The measured median b is 26.4 km s^{-1} , while OCDM predicts 23.6 km s^{-1} .

The AutoVP analysis of the spectrum of Q1937–1009 yielded a total of 495 absorption features. The expected numbers of lines predicted by the models are for CHDM: 469.8; ΛCDM_L : 518.8; ΛCDM_H : 520.8; OCDM: 504.6; SCDM: 535.0, and tCDM: 501.2, all of which are consistent with the measured number, within Poisson fluctuations.

For both the N_{HI} and b distributions, we find that the probability distribution for $N^{1/2}d_{\text{KS}}$, where N is the number of absorption lines, is narrower than the theoretical distribution, so that the rejection probabilities provided by the KS test are perhaps conservative. We discuss this further in Appendix A.

Allowing for an offset in the continuum level as pre-

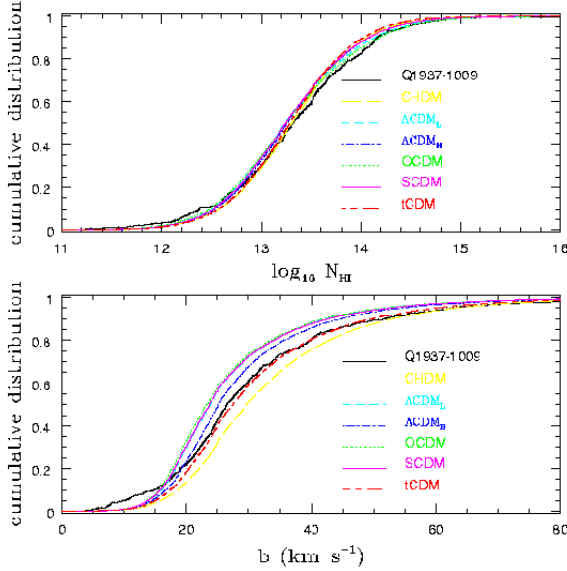


Figure 8. Comparison between the measured absorption line parameter cumulative distributions of Q1937–1009 and the model predictions using AutoVP, allowing for an offset in the continuum level. The predicted N_{HI} distributions tighten about the measured distribution. The tCDM model now agrees best with the measured b -distribution.

viously has only a small effect on the N_{HI} distributions, but does tighten them about the measured distribution, as shown in Figure 8. The best-fitting model is OCDM, for which $d_{\text{KS}} = 0.062$ and $P_{\text{KS}} = 0.043$. The other models give for CHDM: $d_{\text{KS}} = 0.064$, $P_{\text{KS}} = 0.036$; $\Lambda\text{CDM}_{\text{L}}$: $d_{\text{KS}} = 0.067$, $P_{\text{KS}} = 0.024$; $\Lambda\text{CDM}_{\text{H}}$: $d_{\text{KS}} = 0.064$, $P_{\text{KS}} = 0.033$; SCDM: $d_{\text{KS}} = 0.069$, $P_{\text{KS}} = 0.018$; tCDM: $d_{\text{KS}} = 0.072$, $P_{\text{KS}} = 0.012$. All of the models provide a reasonably good match to the measured N_{HI} distribution. By contrast, introducing a continuum offset has a much larger effect on the b -distribution, shifting the best-fitting model from $\Lambda\text{CDM}_{\text{H}}$ to tCDM. For tCDM, $d_{\text{KS}} = 0.060$ and $P_{\text{KS}} = 0.054$, while for $\Lambda\text{CDM}_{\text{H}}$, the next best-fitting model, $d_{\text{KS}} = 0.076$ and $P_{\text{KS}} = 0.007$. The median Doppler b predicted by $\Lambda\text{CDM}_{\text{H}}$ is 25.1 km s^{-1} . The $\Lambda\text{CDM}_{\text{L}}$ model, which provides the best fit to the flux distribution and nearly as good a fit to the N_{HI} distribution as does OCDM, predicts a median b of 23.8 , about 10% below the measured median.

The expected numbers of lines for the models are for CHDM: 473.6; $\Lambda\text{CDM}_{\text{L}}$: 514.0; $\Lambda\text{CDM}_{\text{H}}$: 516.3; OCDM: 502.1; SCDM: 534.7, and tCDM: 507.6. These are nearly identical to the expected numbers predicted for no offset.

To test the sensitivity of the distributions of absorption line parameters to the method of absorption line analysis, we perform a second set of analyses using SPECFIT.

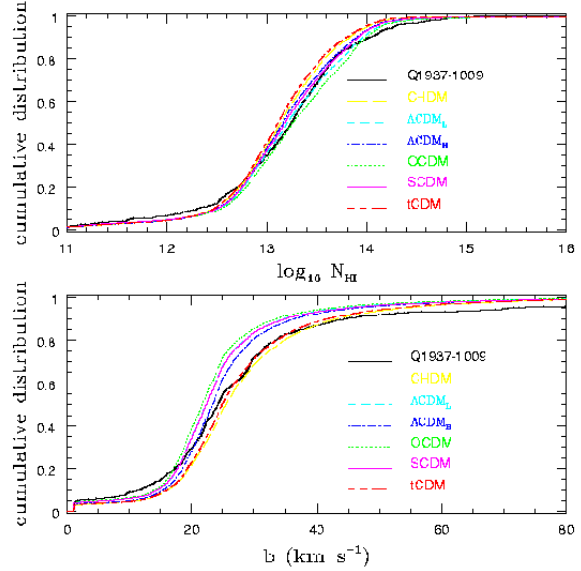


Figure 9. Comparison between the measured absorption line parameter cumulative distributions of Q1937–1009 and the model predictions using SPECFIT. The CHDM and tCDM models are steeper than the observed N_{HI} distribution. None of the models provides a good match to the measured b -distribution, although the CHDM and tCDM models do best.

The results are shown in Figures 9 and 10. The adopted threshold optical depth for finding lines was $\tau_{\text{min}} = 0.15$, although smaller optical depth lines may result from the fits. (It would have been possible to use a smaller value for τ_{min} for most of the models; the value adopted was required by the CHDM and tCDM models to avoid finding an excess number of lines. The same value was adopted for the analysis of all the models for consistency.) The best fits to the measured N_{HI} distribution are provided by the $\Lambda\text{CDM}_{\text{L}}$ and SCDM models. The predicted CHDM and tCDM N_{HI} distributions, not allowing for a continuum offset, do most poorly, both being steeper than the measured distribution. In the absence of a continuum offset, the KS test applied to the $\Lambda\text{CDM}_{\text{L}}$ and SCDM results gives, respectively, $d_{\text{KS}} = 0.045$, $P_{\text{KS}} = 0.16$ and $d_{\text{KS}} = 0.057$, $P_{\text{KS}} = 0.040$. Allowing for a continuum offset gives for the same models, respectively, $d_{\text{KS}} = 0.048$, $P_{\text{KS}} = 0.12$ and $d_{\text{KS}} = 0.043$, $P_{\text{KS}} = 0.20$. The remaining models (with continuum offsets) do significantly more poorly, giving for CHDM: $d_{\text{KS}} = 0.071$, $P_{\text{KS}} = 0.004$; $\Lambda\text{CDM}_{\text{H}}$: $d_{\text{KS}} = 0.056$, $P_{\text{KS}} = 0.041$; OCDM: $d_{\text{KS}} = 0.073$, $P_{\text{KS}} = 0.003$; tCDM: $d_{\text{KS}} = 0.082$, $P_{\text{KS}} = 6 \times 10^{-4}$. In contrast to the AutoVP analysis, which gives OCDM as the best-fitting model, the N_{HI} distribution derived for OCDM using SPECFIT provides a poor match to the data.

As was found in the AutoVP analysis, there is an ex-

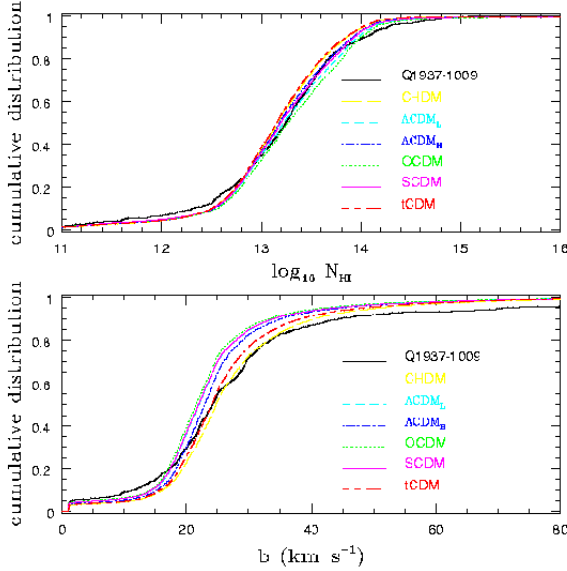


Figure 10. Comparison between the measured absorption line parameter cumulative distributions of Q1937–1009 and the model predictions using SPECFIT, allowing for an offset in the continuum level. The predicted N_{HI} and b distributions tighten.

cess of low b -value systems in the data over the models. None of the models particularly well represents the measured b -distribution, although the CHDM and tCDM do best, both in the absence or presence of continuum offsets. The CHDM and tCDM models, when continuum offsets are allowed for, give, respectively, $d_{\text{KS}} = 0.081$, $P_{\text{KS}} = 7 \times 10^{-4}$ and $d_{\text{KS}} = 0.080$, $P_{\text{KS}} = 9 \times 10^{-4}$. The other models produce too narrow lines. This is in contrast to AutoVP, which finds that the $\Lambda\text{CDM}_{\text{H}}$ model better fits the measured distribution when no continuum offset is assumed. When continuum offsets are allowed for, however, SPECFIT favours tCDM, as does AutoVP, although SPECFIT rejects the model with a much higher level of confidence. The measured median b -value using SPECFIT is 24.2 km s^{-1} , somewhat smaller than found by AutoVP. The SPECFIT prediction for $\Lambda\text{CDM}_{\text{L}}$ (allowing for a continuum offset), is a median b of 22.1 km s^{-1} , smaller than the measured value by 10%, similar to the discrepancy found using AutoVP. It appears difficult to reach any definite conclusion regarding the goodness-of-fit of the predicted Doppler parameter distributions to the data. It is possible the two algorithms cue off low optical depth fluctuations differently. The main lesson to be drawn is likely that there is a limit to the physical interpretation of gas temperature or velocity dispersion that may be attached to the fit Doppler parameters.

The SPECFIT analysis of the spectrum of Q1937–1009 found 609 absorption features. The expected numbers of

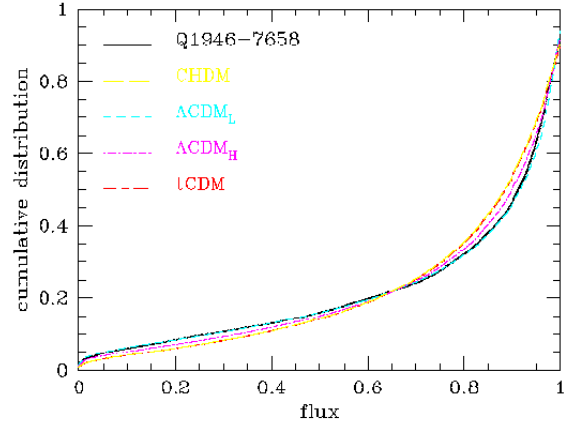


Figure 11. Comparison between the measured flux distribution of Q1946+7658 and the model predictions. A continuum offset was applied to each model to enforce matching the cumulative distributions at flux values near unity. The preferred models are $\Lambda\text{CDM}_{\text{L}}$ and $\Lambda\text{CDM}_{\text{H}}$.

lines predicted by the models are for CHDM: 695.7; $\Lambda\text{CDM}_{\text{L}}$: 585.4; $\Lambda\text{CDM}_{\text{H}}$: 654.9; OCDM: 530.3; SCDM: 607.5, and tCDM: 718.1. Allowing for Poisson fluctuations, all the model predictions are consistent with the measured number except for CHDM and tCDM, although the OCDM model is marginal.

3.2 Q1946+7658

3.2.1 Flux distribution

Over the redshift range $2.5 < z < 3.0$, the mean optical depth is found to be $\bar{\tau}_{\alpha} = 0.24$. Recent CMB experiments strongly favour a flat, or nearly flat, universe (de Bernardis et al. 2000). From hereon, we restrict the consideration of models to those currently most viable: CHDM, the two ΛCDM models, and tCDM. Although the tCDM model is perhaps already excluded by the CMB data, it provides useful comparisons with the predictions of the CHDM model and illustrates the degree to which models of the Ly α forest may (or may not) discriminate between cosmological models. The adopted optical depth rescalings for these models are provided in Table 4. No additional evolution in the UV background was required ($p = 0$).

The distributions of flux per pixel are shown in Figure 11. The best-fitting models are $\Lambda\text{CDM}_{\text{L}}$ and $\Lambda\text{CDM}_{\text{H}}$,

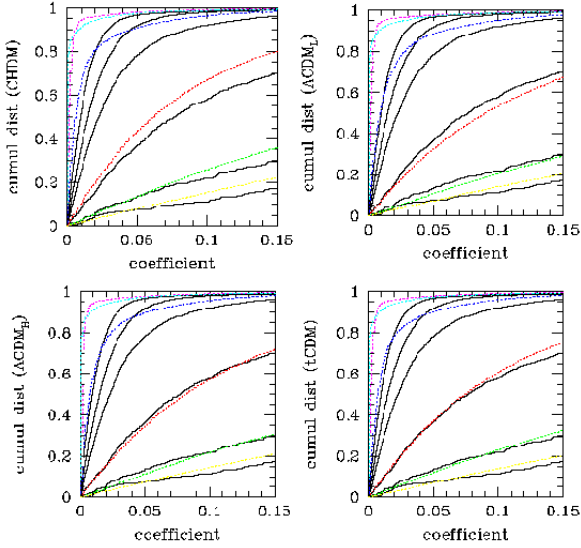


Figure 12. Comparison between the measured wavelet coefficient cumulative distributions of Q1946+7658 (solid curves) and the model predictions (dotted curves), allowing for continuum offset corrections. The curves from left to right correspond to the velocity scales 2–4 km s^{−1}, 4–8 km s^{−1}, 8–16 km s^{−1}, 16–32 km s^{−1}, 32–64 km s^{−1}, and 64–128 km s^{−1}. The best match for the velocity scales 16–32 km s^{−1}, corresponding to the median velocity width of the absorption features, is found for the Λ CDM_H and tCDM models. All the models underpredict the amount of velocity structure on smaller scales.

with the respective maximum cumulative distributions differences from that measured of $d_{\text{KS}} = 0.039$ and $d_{\text{KS}} = 0.038$, and respective KS test acceptance probabilities of $P_{\text{KS}} = 6 \times 10^{-23}$ and $P_{\text{KS}} = 2 \times 10^{-21}$. The values of d_{KS} are far in excess of the expected values for the $\sim 1.7 \times 10^4$ pixels of the measured spectrum, although the low formal KS probabilities attached to the values appear to be underestimates of the true values, as discussed in Appendix A.

3.2.2 Wavelet coefficient distributions

The wavelet coefficient distributions are shown in Figure 12. All the models poorly match the velocity structure on scales of 8–16 km s^{−1} and smaller. The best agreement on larger scales is provided by the Λ CDM_H and tCDM models. Good agreement continues to be found on larger velocity scales.

3.2.3 Absorption line parameter distributions

All the models underpredict the number of H I column density systems with $N_{\text{HI}} < 10^{13} \text{ cm}^{-2}$, as shown in Figure 13.

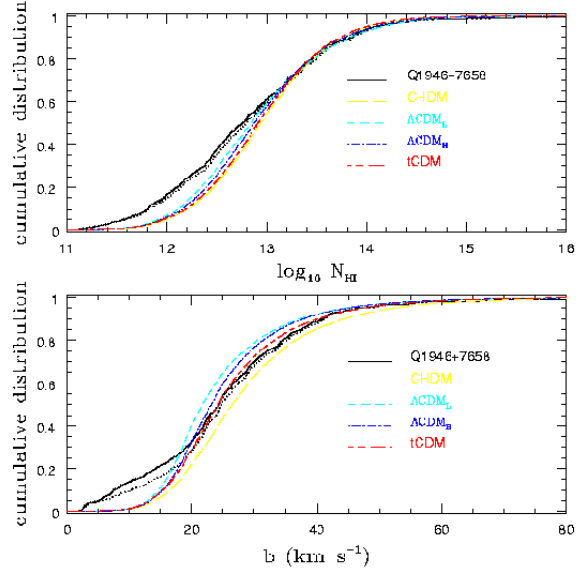


Figure 13. Comparison between the measured absorption line parameter distributions of Q1946+7658 (solid curves) and the model predictions. While good agreement is generally found for the N_{HI} distributions above 10^{13} cm^{-2} , all the models underpredict the number of lower column density systems. The tCDM model best reproduces the measured b -distribution. The agreements improve when metal absorption systems identified in the observed spectrum are removed (dotted curves).

The Λ CDM_L model most closely matches the observed distribution at higher values. None of the models provides a particularly good match to the measured b -distribution because of the large tail at $b < 20 \text{ km s}^{-1}$; the tCDM model is closest at larger values.

The AutoVP analysis of the spectrum of Q1946+7658 yielded 471 absorption features. The predicted numbers for the various models are for CHDM: 468.7; Λ CDM_L: 494.0; Λ CDM_H: 497.6; and tCDM: 499.1, all consistent with the measured number within the Poisson error.

It is possible that the low N_{HI} and low b -value systems in the measured spectrum are dominated by metal absorption features. Kirkman & Tytler (1997) identify a large number of metal lines in the redshift range analysed. Unfortunately, because these lines are frequently blended with Ly α forest systems, it is not possible to match them on a one-to-one basis with the lines produced by AutoVP. In an attempt to account for the metal absorbers, we remove a narrow line ($b < 15 \text{ km s}^{-1}$) from our list when it matches against a metal absorber in the list of Kirkman & Tytler (1997) to within a tolerance of 2 Å in the line-centre wavelength. This results in the removal of 28 systems. The resulting cumulative distributions, shown by the dotted curves in

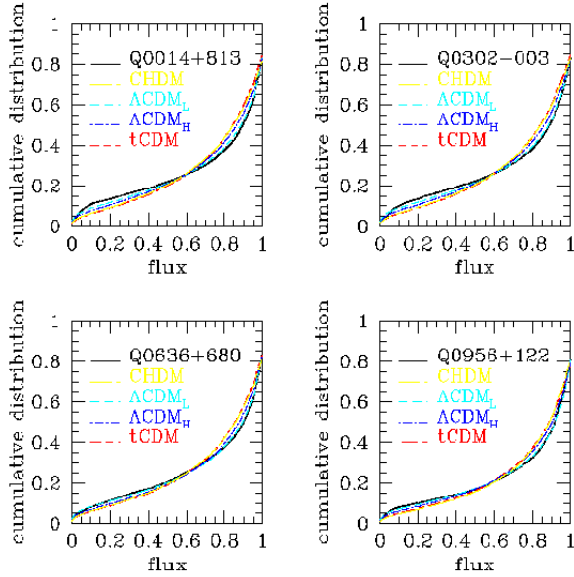


Figure 14. Comparison between the measured flux distributions of the Hu et al. (1995) QSO spectra and the model predictions. A continuum offset was applied to each model to enforce matching the predicted and measured cumulative distributions at flux values near unity. For all spectra, the Λ CDM_L model is the preferred model.

Figure 13, match the predicted more closely, but still are not in good agreement. We return to this point in Section 4 below. We note that as was the case for Q1937–1009, the models that best fit the flux distribution provide too small median Doppler parameters. The measured median b (after excluding metal lines) is 24.8 km s^{-1} , while Λ CDM_L and Λ CDM_H predict, respectively, 21.7 km s^{-1} and 23.1 km s^{-1} .

3.3 Q0014+813, Q0302–003, Q0636+680, Q0956+122

3.3.1 Flux distribution

The analysis redshift ranges for each of the Hu et al. (1995) QSO spectra are given in Table 2. The mean optical depth found for each is: Q0014+813: $\bar{\tau}_\alpha = 0.30$; Q0302–003: $\bar{\tau}_\alpha = 0.31$; Q0636+680: $\bar{\tau}_\alpha = 0.29$; Q0956+122: $\bar{\tau}_\alpha = 0.25$. The predicted model distributions are computed by interpolation between the simulation results at $z = 2$ and $z = 3$ using equation 2. It was found unnecessary to include any amount of additional evolution in the UV radiation background.

The distributions of flux per pixel are shown in Figure 14. The best-fitting model is Λ CDM_L in all cases. The predicted distributions, however, fit the measured distributions only moderately well to poorly. The maximum

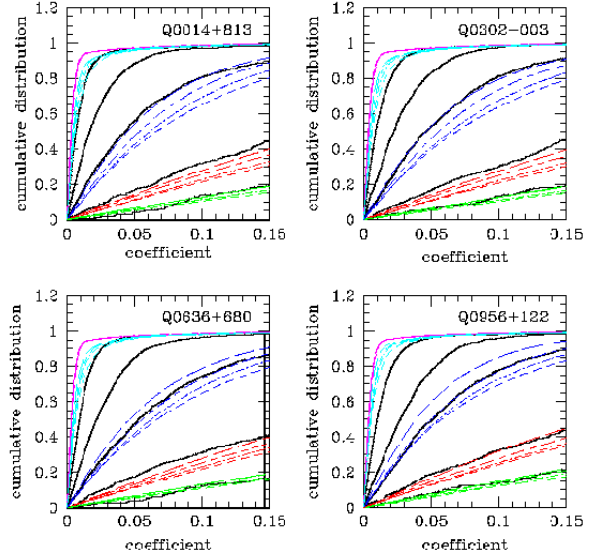


Figure 15. Comparison between the measured wavelet coefficient cumulative distributions of the Hu et al. (1995) QSO spectra (heavy solid curves) and the model predictions, allowing for continuum offset corrections. The curves from left to right correspond to the approximate velocity scales $4\text{--}8 \text{ km s}^{-1}$, $8\text{--}16 \text{ km s}^{-1}$, $16\text{--}32 \text{ km s}^{-1}$, $32\text{--}64 \text{ km s}^{-1}$, and $64\text{--}128 \text{ km s}^{-1}$. Model predictions are shown for CHDM (long-dash), Λ CDM_L (short dash), Λ CDM_H (dot – short dash), and tCDM (short dash – long dash). The best match for the velocity scales $16\text{--}32 \text{ km s}^{-1}$, corresponding to the median velocity width of the absorption features, is found for the CHDM and tCDM models. All the models underpredict the amount of velocity structure on smaller scales.

differences between the measured cumulative distributions and those predicted for the Λ CDM_L model, and associated KS test probabilities, are for Q0014+813: $d_{\text{KS}} = 0.022$, $P_{\text{KS}} = 6 \times 10^{-4}$; Q0302–003: $d_{\text{KS}} = 0.021$, $P_{\text{KS}} = 0.002$; Q0636+680: $d_{\text{KS}} = 0.015$, $P_{\text{KS}} = 0.05$; and Q0956+122: $d_{\text{KS}} = 0.030$, $P_{\text{KS}} = 10^{-6}$. (The values of P_{KS} , however, may underestimate the true probabilities. See Appendix A.)

3.3.2 Wavelet coefficient distributions

The wavelet coefficient distributions are displayed in Figure 15. All the models poorly match the measured velocity structure on scales of $4\text{--}8 \text{ km s}^{-1}$ and $8\text{--}16 \text{ km s}^{-1}$. The best agreement on the scales of $16\text{--}32 \text{ km s}^{-1}$ and larger is provided by the CHDM and tCDM models.

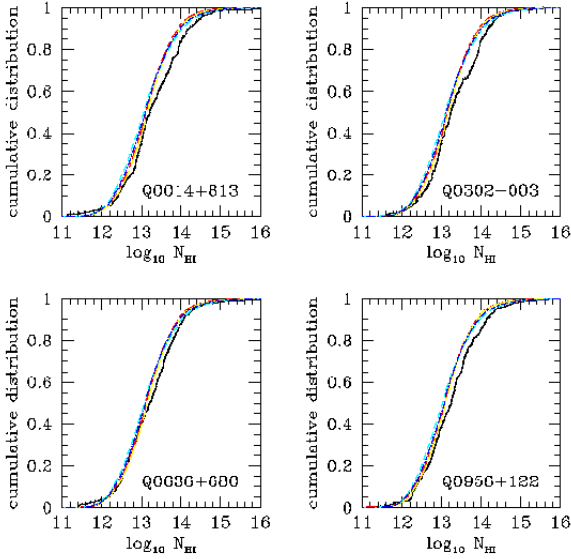


Figure 16. Comparison between the H I column density distributions measured using the Hu et al. (1995) QSO spectra and the model predictions. The curves are labelled as in Figure 15. All the models predict a steeper distribution than measured.

3.3.3 Absorption line parameter distributions

The H I column density and Doppler parameter distributions for the QSO spectra of Hu et al. (1995) are shown in Figures 16 and 17 along with the model predictions. All the models predict an H I column density distribution and Doppler parameter distribution that both peak at lower values than measured. Of the 4 QSO spectra, the N_{HI} distributions for only Q0636+680 and Q0956+122 are well-represented by any of the models. The predictions of CHDM, the best-fitting model, for the N_{HI} distribution of Q0636+680 gives $d_{\text{KS}} = 0.074$ and $P_{\text{KS}} = 0.083$, while for Q0956+122 the predictions give $d_{\text{KS}} = 0.10$ and $P_{\text{KS}} = 0.011$. For Q0014+813, the best-fitting model is CHDM with $d_{\text{KS}} = 0.11$ and $P_{\text{KS}} = 0.004$, while for Q0302-003 ΛCDM_L provides the best fit with $d_{\text{KS}} = 0.12$ and $P_{\text{KS}} = 0.001$. None of the models is able to match the high b -values found in the data very well. The ΛCDM model is closest for Q0636+680 with $d_{\text{KS}} = 0.091$ and $P_{\text{KS}} = 0.018$, and the CHDM model is closest for Q0956+122 with $d_{\text{KS}} = 0.11$ and $P_{\text{KS}} = 0.004$. As found for Q1937-1009 and Q1946+7658, the model which best agrees with the measured flux distribution produces too small a median b . The measured median Doppler parameters for Q0014+813, Q0302-003, Q0636+680, and Q0956+122 are, respectively, 30.5 km s^{-1} , 29.5 km s^{-1} , 25.6 km s^{-1} , and 28.0 km s^{-1} . The predictions of ΛCDM_L range between $20\text{--}21 \text{ km s}^{-1}$ for all the QSOs, too low by $20\text{--}50\%$.

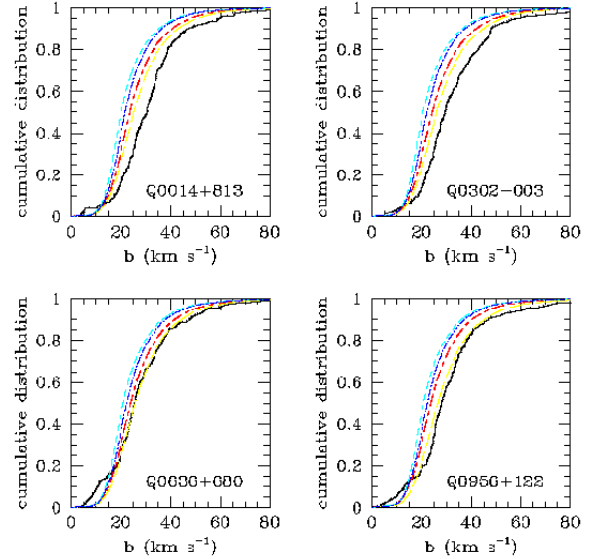


Figure 17. Comparison between the Doppler parameter distributions measured using the Hu et al. (1995) QSO spectra and the model predictions. The curves are labelled as in Figure 15. All the models predict a distribution peaking at lower values than measured.

The AutoVP analyses of Q0636+680 and Q0956+122 find 287 and 239 lines, respectively. The CHDM model predicts 316.7 and 288.2 lines, respectively, somewhat higher than the measured numbers. The respective predictions of ΛCDM are 340.2 and 307.8, which exceed the measured numbers by $3\text{--}4\sigma$.

We note that Hu et al. (1995) reported a significantly larger number of narrow absorption features in the spectrum of Q0636+680 than in any of the other spectra, and that most of these could be identified with metal lines (13 lines in the redshift range analysed here). They consequently excluded Q0636+680 from their statistics of the Ly α forest. We similarly find a larger number of narrow lines ($b < 10 \text{ km s}^{-1}$) in Q0636+680 compared with the other spectra. The flux and N_{HI} distributions, however, show no anomalous behaviour compared with the other 3 spectra, and in fact these distributions, along with the b -distribution, agree better with the model predictions than the distributions found for any of the other QSO spectra. The amount of metal line contamination based on the tabulations in Hu et al. (1995) is small (5% of the lines in Q0636+680, 2% in Q0956+122, no lines in Q0014+813 and 1 line in Q0302-003). Nonetheless, many of the narrow absorption features may be unidentified metal lines.

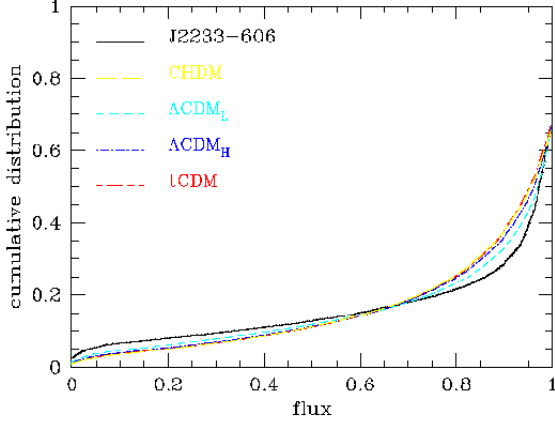


Figure 18. Comparison between the measured flux distribution of J2233–606 and the model predictions. A continuum offset was applied to each model to enforce matching the cumulative distributions at flux values near unity. None of the models recovers the measured flux distribution, although the Λ CDM_L model is closest.

3.4 J2233–606

3.4.1 Flux distribution

The mean optical depth for J2233–606 is $\bar{\tau}_\alpha = 0.16$ over the analysis redshift interval $1.732 < z < 2.132$. The rescaling parameters used are given in Table 5. The simulation results at only $z = 2$ are used to extrapolate over the analysis redshift range, using the values for α from Table 4. It was found unnecessary to include any additional amount of evolution in the UV radiation background.

The distributions of flux per pixel are shown in Figure 18. All of the models differ greatly from the data; the Λ CDM_L model is closest.

3.4.2 Wavelet coefficient distributions

The wavelet coefficient distributions are shown in Figure 19. All the models poorly match the velocity structure on scales of 7–13 km s^{−1} and smaller. The best agreement on the 13–27 km s^{−1} scales is provided by the CHDM model. The models fail to recover the measured behaviour at larger velocity scales.

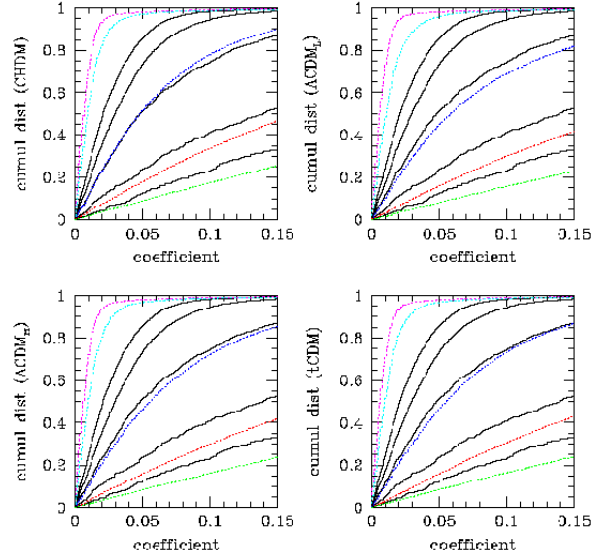


Figure 19. Comparison between the measured wavelet coefficient cumulative distributions of J2233–606 (solid curves) and the model predictions (dotted curves), allowing for continuum offset corrections. The curves from left to right correspond to the approximate velocity scales 4–7 km s^{−1}, 7–13 km s^{−1}, 13–27 km s^{−1}, 27–54 km s^{−1}, and 54–108 km s^{−1}. The best match for the velocity scales 13–27 km s^{−1}, corresponding to the median velocity width of the absorption features, is found for the CHDM model. All the models underpredict the amount of velocity structure on smaller scales.

3.4.3 Absorption line parameter distributions

Despite the poor agreement with the measured flux distribution, all the models well reproduce the N_{HI} distribution, as shown in Figure 20. The best agreement is given by the Λ CDM_L model, with $d_{\text{KS}} = 0.046$ and $P_{\text{KS}} = 0.74$. The model predictions for the b -distributions agree poorly with that measured. The Λ CDM_L model again does best, with $d_{\text{KS}} = 0.15$ and $P_{\text{KS}} = 0.001$. Using the line list of Cristiani & D’Odorico (2000), we match 28 of the narrow lines found to metal lines. After these lines are removed, the agreement between the resulting b distribution and the model predictions greatly improves, with the best model CHDM, for which $d_{\text{KS}} = 0.075$ and $P_{\text{KS}} = 0.22$. As was found for all the previous QSO spectra, Λ CDM_L underpredicts the measured median Doppler parameter. The measured median is 24.7 km s^{−1}, while Λ CDM_L predicts 20.0 km s^{−1}.

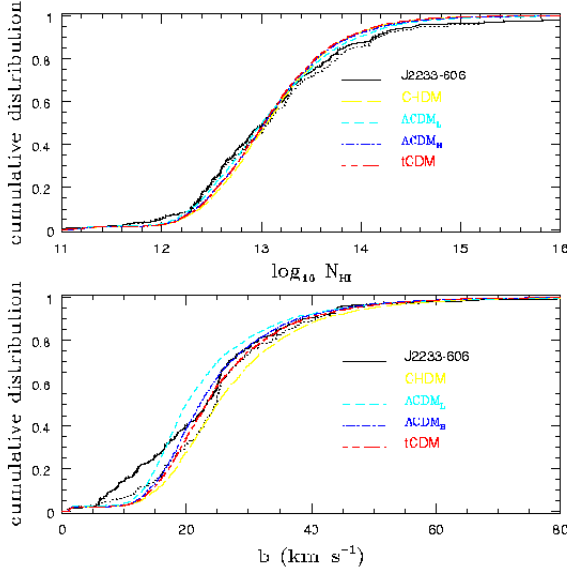


Figure 20. Comparison between the measured absorption line parameter distributions of J2233–606 and the model predictions. The dotted lines show the measured distributions once identified metal lines have been removed.

4 DISCUSSION

In this section, we consider the possible systematics and limitations of each of the tests used, and discuss what may still be concluded from the comparison between the models and the data. No single cosmological model clearly emerges as the best based on the full set of statistical tests. The measured distributions of flux per pixel are the most easily reproduced. The cumulative distribution of flux predicted by the Λ CDM_L model agrees with the distribution measured in Q1937–1009 to an accuracy of $d_{\text{KS}} = 0.013$, close to the level of precision of the simulation (see Appendix A). For Q1946+7658, the Λ CDM_L and Λ CDM_H model predicted distributions both agree with that measured with $d_{\text{KS}} < 0.04$. Similar levels of agreement are found for the other QSO spectra except for J2233–606. The reason for the poor agreement in the latter is unclear, but it may in part be due to the low redshift of the QSO ($z_{\text{em}} = 2.238$). At such low redshifts, the simulation volume is beginning to become non-linear. Consequently we shall focus the discussion on the higher redshift QSO analyses.

Part of the reason for the high degree of accuracy in the agreement is the large number of pixels. The theoretically expected value of d_{KS} for N independent measurements is $\bar{d}_{\text{KS}} \simeq 0.9/N^{1/2}$, and d_{KS} should exceed $1.6/N^{1/2}$ only 1% of the time. For a typical number of pixels $N \sim 10^4$, the agreement between the predicted and measured cumu-

lative flux distributions should then be $d_{\text{KS}} \approx 0.01$. In practice, the probability distribution of d_{KS} is broader than the theoretical distribution (see Appendix A). Nonetheless, the variance in d_{KS} for a given model is small compared with the spread between models, so that it may still serve as a basis for distinguishing the models. The models which fare most poorly are CHDM and tCDM. The reason is essentially due to their lower power spectra normalizations. In terms of σ_{34} , the power on the wavevector scale $34\Omega_0^{1/2}h \text{ Mpc}^{-1}$, the normalization that best reproduces the measured flux distribution of Q1937–1009 (Figure 3), is $\sigma_{34} = 2.03$ (M00, for Λ CDM_L using the power spectrum at $z = 3$). The remaining models do increasingly poorly as the normalization is increased (OCDM: $\sigma_{34} = 2.50$) or decreased (sCDM: $\sigma_{34} = 1.89$; Λ CDM_H: $\sigma_{34} = 1.54$). The CHDM and tCDM models do about equally poorly with the lowest normalizations, $\sigma_{34} = 1.14$ and 1.09 , respectively. Because the flux distributions are sensitive to the intensity of the H I ionizing UV background, they provide constraints on the amplitude of the background, within the context of the models. We discuss the implications for the origin of the ionizing background below.

For a typical number of lines of $N \sim 500$, the average difference between the predicted and measured cumulative distributions of the absorption line parameters should be $\bar{d}_{\text{KS}} \approx 0.04$, comparable to the differences found. This is close to the differences between models predicted for the N_{HI} distributions, and so cannot serve to discriminate between models on the basis of a single QSO spectrum. With 10–20 spectra, however, the N_{HI} distribution should provide an additional constraint on models. The differences between the model predictions for the b distributions are greater, and so a single QSO spectrum could in principle be used as a discriminator between models. In practice, uncertainties in the continuum level render the b distribution less useful, since small continuum offsets can cause shifts between the best-fitting model. The N_{HI} distribution, in contrast, is less sensitive to continuum uncertainties. A second source of difficulty in using the line parameter distributions are systematic differences found between the model predictions and the measured distributions. The measured N_{HI} distributions generally show a tail of low N_{HI} systems for $\log N_{\text{HI}} < 12.5$ that are not found in the simulations. Similarly, a larger number of low b -value systems are consistently found in the data compared with the model predictions. The low b -values are obtained regardless of the absorption line-analysis algorithm used. They are confirmed by the wavelet analyses, showing that these narrow systems are not artefacts of the line-analysis routines. We discuss the possible implications of these differences between the model predictions and the measured distributions below.

4.1 Evolution of Γ

Since the gas is in photoionization equilibrium, the optical depth in Ly α is predicted by the models only to within a factor of $b_{\text{ion}} \propto \Omega_b^{1.6}/\Gamma$, where Γ is the H I photoionization rate provided by the UV background. The re-normalizations of the optical depths required for a given model to match the measured mean optical depth in Ly α for a QSO spectrum provides an estimate of the value of Γ required for the model to match the spectrum.

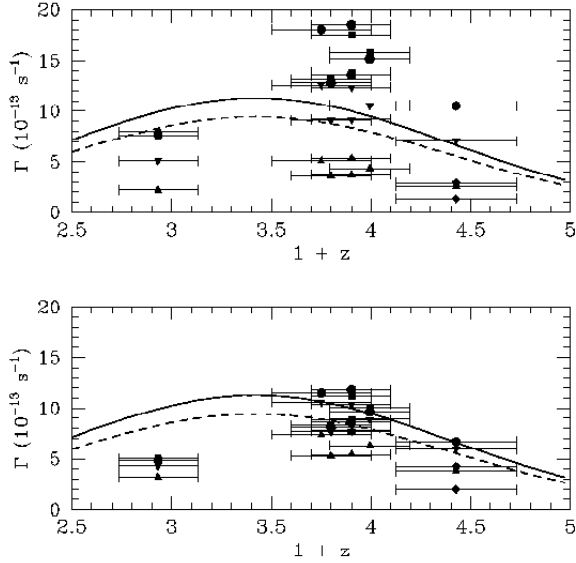


Figure 21. Required H I photoionization rate Γ required for the models to match the measured mean optical depths, for CHDM (circles), Λ CDM_L (triangles), Λ CDM_H (inverted triangles), tCDM (squares), OCDM (diamonds), and SCDM (pentagons). The upper panel shows Γ for the value of Ω_b assumed in the model. The lower panel shows Γ assuming a fixed value of $\Omega_b h^2 = 0.019$ for all the models. The predicted values are close to the estimated Γ from QSO sources alone for an intrinsic QSO spectral index of $\alpha_Q = 1.5$ (solid curve) and $\alpha_Q = 1.8$ (dashed curve).

In Figure 21 we show the required values of Γ for the models to match the measured mean optical depth $\bar{\tau}_\alpha$ in each QSO spectrum. Two estimates are made. For the first, we show the values of Γ assuming the value for Ω_b adopted in each model. For the second, we show the values of Γ assuming $\Omega_b h^2 = 0.019$ (Burles & Tytler 1998) after rescaling the optical depths by b_{ion} . The scatter is considerably reduced in the latter case. Also shown are the theoretical predictions for Γ for QSO sources alone, assuming an intrinsic QSO spectral index of $\alpha_Q = 1.5$ or 1.8 (Haardt & Madau 1996). The required values of Γ are found to lie close to the predicted rates, suggesting little, if any, sources in addition to QSOs are required, or are even permitted without destroying the agreement between the models and the measured spectra. We note, however, that the rate of evolution of Γ required to match the measurements of the mean optical depth over the redshift range probed by the spectrum of Q1937–1009 ($3.1 < z < 3.7$) was found to be significantly slower than given by Haardt & Madau (1996). The difference may be due to the uncertainty in the QSO counts at these high redshifts.

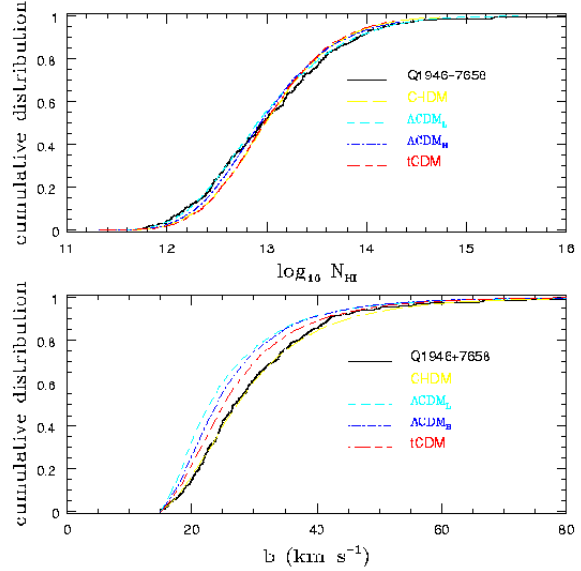


Figure 22. Comparison between the measured absorption line parameter distributions of Q1946+7658 with all $b < 15 \text{ km s}^{-1}$ systems removed from the data (solid curves) and from the model predictions. The agreement is substantially improved over the case when all systems are included for both the N_{HI} and b distributions (compare with Figure 13). The CHDM model now provides the best match to the b distribution, while all the models provide acceptable fits to the N_{HI} distribution.

4.2 Absorption line parameter distributions

Although the model predictions for the N_{HI} and b distributions show generally good agreement with the measured distributions, the comparisons show discrepancies that are common to all the analyses: a tail of low N_{HI} and low b -value systems in the data compared with the models, and a higher measured median b -value than provided by the best-fitting model to the flux distribution.

It is clear that part of the discrepancy at low N_{HI} and low b is due to metal line contamination in the measured spectra. The line lists compiled in the literature, however, are not able to account fully for the discrepancies. The discrepancy is particularly apparent in the analysis of Q1946+7658, for which it was shown that the metal lines identified by Kirkman & Tytler (1997) account for only about a third of the narrow systems. This is likely due in part to the difficulty of matching the positions of the metal lines they found in their analysis compared with the AutoVP results here because of the differences in the absorption line fitting procedures. Although we matched 28 metal lines, Kirkman & Tytler (1997) report 45 in the redshift range analysed, which could potentially account for half the

discrepancy for both the N_{HI} and b distributions due to the narrowness and the small equivalent widths of the metal systems.

These discrepancies, whether or not due to metal lines, are linked, as may be demonstrated by excluding all systems with $b < 15 \text{ km s}^{-1}$ from the measured and model cumulative distributions. The results are shown in Figure 22. Excluding the low b -value systems eliminates the $\log N_{\text{HI}} < 13$ tail. This suggests that the discrepancy may be due entirely to metal absorption systems, but is not conclusive. The number of such lines would be large: 99 lines of the original 471 found by AutoVP have $b < 15 \text{ km s}^{-1}$, so that a large fraction of them would have to be unidentified metal lines. An alternative may be that many of these systems are genuine Ly α forest absorbers located in under-dense regions. According to Zhang et al. (1998), these systems tend to be both narrow and have low H I column densities. Their densities are so low that they are not able to maintain thermal balance against adiabatic expansion (Meiksin 1994). If these systems were photoionized earlier than assumed in the simulation ($z_{\text{ion}} = 6$), the additional Compton cooling may be able to substantially lower their temperatures. Although this would assist in producing narrow lines, it is unclear that additional cooling would be adequate. The results of Zhang et al. (1998) show that the b -parameters of these systems are due in large part to velocity broadening. It is not possible to address this issue without further simulations, so that the prevalence of the narrow lines in the data remains incompletely explained by the models at this time.

The Doppler parameter distributions show a second discrepancy with the simulations: the models that best fit the flux distributions predict smaller median b -values than measured. For instance, while the $\Lambda\text{CDM}_{\text{L}}$ model best matches the flux distribution of Q1937–1009, the b -distribution is best matched by $\Lambda\text{CDM}_{\text{H}}$ or tCDM. The median Doppler parameter predictions of $\Lambda\text{CDM}_{\text{L}}$ fall short of the measured median values by 10–50%, depending on the spectrum. The flux distribution was found above to be primarily sensitive to the normalization of the primordial power spectrum, with lower values of σ_{34} than in the $\Lambda\text{CDM}_{\text{L}}$ model producing increasingly poorer agreement with the data. By contrast, the median b values increase with decreasing power (Hui & Rutledge 1999; Bryan & Machacek 2000). Thus the greater frequency of broad lines found in the data than predicted by $\Lambda\text{CDM}_{\text{L}}$ favours a lower normalization of the power spectrum, and so conflicts with the normalization required by the flux distribution. The $\Lambda\text{CDM}_{\text{H}}$ model matches the b -distributions better than does $\Lambda\text{CDM}_{\text{L}}$ both because of its lower normalization and somewhat higher baryon density, but also because an additional amount of heating has been added (by increasing the He II heating rate by a factor of 1.8). Yet even this is not always sufficient to match the data, which are better fit by the tCDM or CHDM models (eg Q1946+7658 or the Hu et al. [1995] spectra), which predict flux distributions that agree poorly with the data.

What is the origin of this discrepancy? Possibly a compromise cosmological model may be found which fits all the distributions. For instance, doubling the baryon density for $\Lambda\text{CDM}_{\text{L}}$ from $\Omega_b h^2 = 0.015$ to 0.03 would increase the gas temperature by 40%, using the temperature-baryon density scaling found by Zhang et al. (1998). This may increase the median Doppler parameter by as much as 10–20%, depend-

ing on the contribution of peculiar velocity broadening to the line widths. Although such a high baryon density conflicts with the deuterium abundance determinations of Burles & Tytler (1998) within the context of standard Big Bang Nucleosynthesis, it is consistent with reported CMB measurements of the acoustic peaks (de Bernardis et al. 2000).

It is also possible that the discrepancy is due to the accumulation of various small errors, both in the observations and the simulations. It was shown in the previous section that the b -distributions are sensitive to possible errors in the continuum determination at a level comparable to the differences between models. In Appendix A, it was also shown that the accuracy to which the distributions may be interpolated between the simulation redshift dumps approaches the differences between models. To estimate the possible impact of this uncertainty on the distributions, we adjust the model cumulative distributions in Figure 7 by the error found in Appendix A in the interpolation of the $\Lambda\text{CDM}_{\text{H}}$ model at $z = 3.6$. The resulting distributions differ only slightly from those shown in Figure 7, somewhat increasing the excess tail in the N_{HI} distribution of the data compared with the models near $\log N_{\text{HI}} = 12.5$ and increasing the tail in the b distribution near $b = 20 \text{ km s}^{-1}$, so that the error in interpolation appears not to be responsible for the discrepancy.

There is an issue of convergence of the simulation results, particularly for the b -distribution. Bryan et al. (1999) found that the b -values tended to decrease with increasing spatial resolution of the simulations, although they were able to explore the trend only for a limited range of box sizes. Meiksin & White (2000) expanded the box size and resolution ranges by performing pseudo-hydrodynamical N -body simulations of the Ly α forest. They found that convergence was particularly difficult to achieve in the distribution of wavelet coefficients on the scales of $16 - 32 \text{ km s}^{-1}$ and in the b distributions. The results of their Particle-Mesh simulations suggest that the cumulative distributions may be determined only up to an accuracy of 0.05 – 0.1. The convergence behaviour, however, was found to improve when a pseudo-pressure force was added. They were still unable to reach convergence in the cumulative b distribution to better than about 0.05 even in this case, even allowing for as many as 512^3 grid zones to compute the gravity, a greater number than used in the simulations here. The question of convergence of the full hydrodynamics simulations to such high accuracy we consider as yet unresolved.

Another possibility is that there is missing physics in the simulations. No feedback from galaxy formation has been taken into account. Winds from forming galaxies will inject energy into their surroundings, and so in principle could provide an additional heating source to the gas and so broaden the absorption lines. Whether or not this is possible without severely disturbing the agreement with the N_{HI} distributions is unclear, but we may consider the energetics required to alter the Doppler parameter distribution. We estimate the energy density of the Ly α forest as follows. The combined thermal and kinetic energy per particle in gas giving rise to an absorption feature with a Doppler parameter b is on the order of $\epsilon_p \approx (3/4)m_{\text{H}}b^2$, where m_{H} is the mass of a hydrogen atom. Zhang et al. (1998) find that half the baryons are contained in Ly α absorption systems with $13 < \log N_{\text{HI}} < 15$ at $z > 2$. For an *rms* Doppler parameter of $b \approx 25 \text{ km s}^{-1}$, this gives a total (proper) energy density

in the Ly α forest at $z = 3$ of $\epsilon_{\text{Ly}\alpha} \approx 5 \times 10^{-17} \text{ erg cm}^{-3}$. An increase in the Doppler parameter by 20% would require an increase in the energy density by 40%. We compare this with the possible energy injection by supernovae. For a proper cosmic star formation rate at $z > 3$ of $10 \text{ M}_{\odot} \text{ yr}^{-1} \text{ Mpc}^{-3}$ (Steidel et al. 1999) that has been ongoing for $\sim 10^9 \text{ yr}$, a supernova rate of 1 per 100 M_{\odot} of stars formed, with a kinetic energy of 10^{51} erg per supernova, would be sufficient to produce a kinetic energy density input from star formation of $4 \times 10^{-17} \text{ erg cm}^{-3}$, allowing for an efficiency of 1% for the transfer of the kinetic energy of the supernovae to the IGM. So it is not implausible for feedback from galaxies in the form of supernova-driven winds to stir the IGM sufficiently to produce a significant increase in the widths of the absorption lines. It is possible the narrow ($b < 15 \text{ km s}^{-1}$) absorption systems detected in the QSO spectra, of which some if not all are due to metals, are evidence for supernovae feedback in the form of enriched material. We note that higher heating rates may also be achieved by introducing radiation sources with a harder spectrum than QSOs.

4.3 Gunn-Peterson effect

The original goal of searches for Ly α absorption in the spectra of QSOs was the discovery of intergalactic hydrogen, presumed to be uniformly distributed. The discovery of a uniform component to the IGM has proven largely elusive, although searches continue. These are pursued under a variety of strategies: the search for additional Ly α absorption to what may be accounted for by Ly α forest blanketing alone (Steidel & Sargent 1987), absorption in the spectra between Ly α forest absorption lines (Giallongo, Cristiani, & Trevese 1992), or determinations based on the distribution of pixel flux (Webb et al. 1992; Fang & Crofts 1995). The measurements provide additional constraints on the models presented here. The results of these measurements have generally placed an upper limit on the optical depth of a smooth component of 0.05–0.1, with a few claimed (but model-dependent) detections of this order, over the redshift range $2 < z < 5$.

The models discussed here show that essentially all the structure of the IGM is in the form of fluctuations that give rise to absorption features, even in underdense regions (Zhang et al. 1998), although a residual smooth component may be detectable in minivoids. We may estimate the amount of additional absorption due to a smooth component as the difference $\tau_s = \bar{\tau}_{\alpha} - \tau_{\text{eff}}$, where τ_{eff} is the effective optical depth due to line-blanketing, given over a redshift interval Δz by $\tau_{\text{eff}} = (1/\lambda_{\alpha}) \sum_i w_i^{\text{obs}} / \Delta z$, where the sum is carried over the observed equivalent widths of the lines and λ_{α} is the (rest) wavelength of Ly α (Meiksin & Madau 1993). The mean and effective optical depths measured from the spectra in Table 2 (with metal lines removed as discussed in Section 3) are shown in Figure 23. The differences in optical depth range over $0.01 < \tau_s < 0.05$. The predictions of the ΛCDM_L model are also shown. We find $\tau_s < 0.1$ at $z \simeq 3.5$, diminishing nearly to zero at lower redshift. Thus there is very little absorption present in both the measured and the model spectra that may not be accounted for by the Ly α forest alone. Similar results are found for the other models.

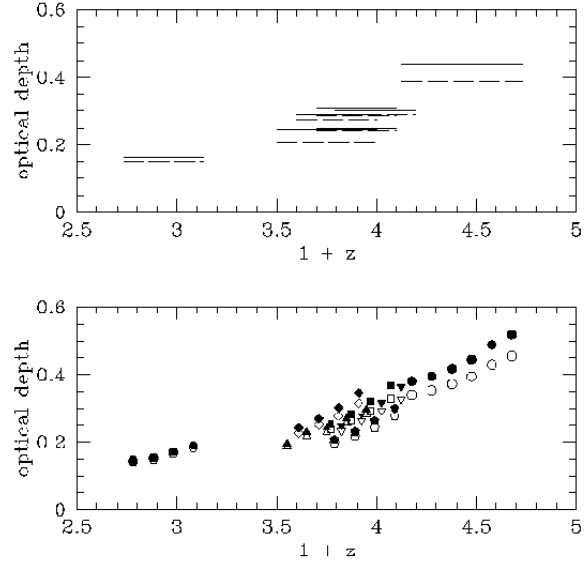


Figure 23. (Upper panel) Comparison between the total mean optical depth $\bar{\tau}_{\alpha}$ (solid lines) and the measured effective optical depth τ_{eff} (dashed lines) due to line-blanketing by the Ly α forest for the QSO spectra in Table 2. (Lower panel) The predictions of the ΛCDM_L model for $\bar{\tau}_{\alpha}$ (solid symbols) and τ_{eff} (open symbols) for the spectra. The points near $z = 3$ have been slightly offset in redshift for clarity. The symbols correspond to Q1937–1009 (circles), Q1946+7658 (triangles), Q0014+813 (inverted triangles), Q0302–003 (squares), Q0636+680 (diamonds), Q0956+122 (pentagons), J2233–606 (hexagons).

5 SUMMARY

We have compared measurements of the Ly α forest in 7 high resolution, high signal-to-noise ratio QSO spectra with predictions of hydrodynamical simulations for a variety of CDM-dominated cosmologies. The comparisons were based on the distribution of flux per pixel and the statistics of the light fluctuations in the spectra as determined by a wavelet analysis and by Voigt profile fitting to absorption features. Although all the models provide reasonably good qualitative descriptions of the measured Ly α forest properties, we find varying levels of agreement with the data depending both on the cosmological model and the basis of comparison. In general, no single model provides a best overall fit in regard to all the tests. We find that the most precise agreement is achieved by the cumulative flux distribution. The predictions of the ΛCDM_L model matches the Ly α forest observed in Q1937–1009 to an accuracy of $d_{\text{KS}} = 0.013$. Either the ΛCDM_L or ΛCDM_H model provides the best fit to the flux distributions of all the remaining QSO spectra. We find that the flux distributions depend primarily on the normalization

of the power spectrum in terms of σ_{34} more so than its shape or the cosmology.

Current CMB measurements strongly favour a flat, or nearly flat, universe. Of 4 flat cosmological models considered, CHDM, two Λ CDM models, and tCDM, the best-fitting model to the H I column density distributions, when the model is at all acceptable ($P_{\text{KS}} > 0.001$), is provided by either CHDM or Λ CDM. (We note that the OCDM results using AutoVP provide a marginally better fit than Λ CDM_L for Q1937–1009, while SPECFIT prefers Λ CDM_L.) The analyses for a few of the QSO spectra do not strongly exclude any of the models. The measured distributions, however, generally show an excess number of low N_{HI} systems compared with the predictions of the simulations. The excess is particularly large in the analysis of Q1946+7658.

The Doppler parameter distributions generally agree most poorly. In no instance does a model reproduce any of the measured distributions with a formal KS probability $P_{\text{KS}} > 0.01$. The measured median Doppler parameters are generally larger than most of the model predictions. The distributions are best fit by CHDM or tCDM, which predict the highest median values. These models also generally provide the best fit to the distribution of wavelet coefficients corresponding to the velocity scale of the median measured Doppler parameter. By contrast, these same models generally produce the poorest fits to the flux distribution. This gives rise to a conflict in the required normalization of the power spectrum. The measured median Doppler parameters favour a low normalization, since the predicted median Doppler parameter increases with decreasing normalization, while the measured flux distributions require a higher normalization than that of the CHDM and tCDM models. The best compromise is Λ CDM_H, although it usually provides the best fit for neither. We find that the measured median Doppler parameter exceeds that predicted by Λ CDM_H by 5–40%, corresponding to an increase in the energy per unit mass of the gas by 10–100%. The size of the discrepancy depends on the spectrum over the same redshift range, although the discrepancy does appear larger at $z < 3$ than at $z > 3$. It is possible that additional sources of heating or turbulent velocity are required, perhaps as may be provided by supernova-driven winds from galaxies, for a model to match both the flux distributions and the Doppler parameter distributions.

A summary of the best-fitting model for each of the tests and QSO spectra is provided in Table 6.

The predicted Doppler parameter distributions generally mismatch the measured distributions also at low values: many more narrow features are found in the data than are predicted. These narrow systems are found also in the distribution of wavelet coefficients, and so are not artefacts of the line fitting algorithms. At $z \sim 3$ they are found to correspond predominantly to the low N_{HI} systems. The most conspicuous cases are Q1946+7658 and J2233–606. Almost all of the narrow systems in J2233–606 may be accounted for by identified metal lines, while only one-third to one-half may be attributed to metal lines in Q1946+7658, and fewer in the remaining spectra. Possible explanations for their existence are that the redshift of ionization is earlier than assumed in the simulations ($z_{\text{ion}} = 6$), permitting additional Compton cooling of under-dense gas, or that the spectra contain a large number of unidentified metal lines. The latter pos-

Model	Ω_0	Ω_Λ	Ω_b	h	n	$\sigma_{8h^{-1}}$
CHDM	1	0	0.07	0.6	0.98	0.7
Λ CDM _L	0.4	0.6	0.0355	0.65	1	1.0
Λ CDM _H	0.4	0.6	0.05	0.65	1	0.8
OCDM	0.4	0	0.0355	0.65	1	1.0
SCDM	1	0	0.06	0.5	1	0.7
tCDM	1	0	0.07	0.6	0.81	0.5

Table 1. Parameters for the cosmological models. Ω_0 is the total density parameter, Ω_Λ the cosmological constant density parameter, Ω_b the baryonic mass fraction, $h = H_0/100 \text{ km s}^{-1} \text{ Mpc}^{-1}$, where H_0 is the Hubble constant at $z = 0$, n the slope of the primordial density perturbation power spectrum, and $\sigma_{8h^{-1}}$ the fluctuation normalization in a sphere of radius $8h^{-1} \text{ Mpc}$.

sibility is particularly intriguing in that the metal systems may be evidence for enrichment by ejecta from the same supernovae which may have heated or stirred the gas through winds.

The requirement that the models match the measured mean optical depths of the Ly α forest places a constraint on the H I photoionization rate. The models presented require an ionization rate that lies within a factor of 2–3 of that predicted for a UV background dominated by QSO sources. A large contribution from additional sources of ionizing radiation would place the models in jeopardy by requiring them to invoke an implausibly high baryon density. We note, however, that the required photoionization background declines at $z > 3.1$ significantly more slowly than predicted by Haardt & Madau (1996) for a background dominated by QSO sources. The mean optical depths obtained by the models are dominated by line-blanketing, with a residual optical depth resulting from a uniform component of at most 0.1 at $z \simeq 3.5$, and becoming vanishingly small by $z \simeq 2$.

ACKNOWLEDGMENTS

This work is supported in part by the NSF under the auspices of the Grand Challenge Cosmology Consortium (GC³). The computations were performed on the Convex C3880, the SGI Power Challenge, and the Thinking Machines CM5 at the National Center for Supercomputing Applications, and the Cray C90 at the Pittsburgh Supercomputing Center under grant AST950004P. A.M. thanks S. Burles and D. Tytler for providing an unpublished electronic version of the spectrum of Q1937–1009. Support for G.L.B. was provided by NASA through Hubble Fellowship grant HF-01104.01-98A from the Space Telescope Science Institute, which is operated by the Association of Universities for Research in Astronomy, Inc., under NASA contract NAS6-26555. M.M. would like to acknowledge the hospitality of the MIT astrophysics group.

QSO	z_{em}	z range	pixel res	spectral res
Q1937–1009	3.806	3.126 – 3.726	7.4×10^4	8.5
Q1946+7658	3.051	2.500 – 3.000	1.5×10^5	7.9
Q0014+813	3.384	2.794 – 3.194	0.06 Å	8.3
Q0302–003	3.286	2.700 – 3.100	0.06 Å	8.3
Q0636+680	3.174	2.600 – 3.000	0.06 Å	8.3
Q0956+122	3.301	2.700 – 3.100	0.06 Å	8.3
J2233–606	2.238	1.732 – 2.132	0.05 Å	6.7

Table 2. The QSO sample. The indicated redshift range is the portion of the spectrum adopted for the analysis. The pixel resolution (as $\lambda/\Delta\lambda$ or pixel width) and spectral resolution (in km s^{-1}), correspond to this region. The observations were reported in: Q1937–1009: Burles & Tytler (1997); Q1946+7658: Kirkman & Tytler (1997); Q0014+813, Q0302–003, Q0636+680, Q0956+122: Hu, Kim, Cowie & Songaila (1995); J2233–606: Cristiani & D’Odorico (2000).

Model	α	p	ω	s
CHDM	6.3	0.0	0	0.3274
CHDM	6.3	5.0	0	0.5525
CHDM	6.3	5.0	0.04	0.63
ΛCDM_L	7.4	0.0	0	1.465
ΛCDM_L	7.4	5.0	0	2.443
ΛCDM_L	7.4	5.0	0.013	2.56
ΛCDM_H	6.8	0.0	0	0.5218
ΛCDM_H	6.8	5.0	0	0.8783
ΛCDM_H	6.8	5.0	0.022	0.94
OCDM	7.4	0.0	0	3.119
OCDM	7.4	4.5	0	4.937
OCDM	7.4	4.5	0.005	4.937
SCDM	7.0	0.0	0	1.291
SCDM	7.0	5.0	0	2.105
SCDM	7.0	5.0	0.018	2.3
tCDM	6.4	0.0	0	0.3076
tCDM	6.4	5.2	0	0.5260
tCDM	6.4	5.2	0.056	0.63

Table 3. Evolution exponents, continuum offsets, and rescaling coefficients for the predicted distributions of optical depth per pixel to match that measured in Q1937–1009. The value for α corresponds to the redshift interval $3 < z < 4$.

Model	α	ω	s
CHDM	6.3	0.03	0.59
ΛCDM_L	6.8	0.005	2.1
ΛCDM_H	6.8	0.015	0.85
tCDM	6.4	0.04	0.59

Table 4. Evolution exponents, continuum offsets, and rescaling coefficients for the predicted distributions of optical depth per pixel to match that measured in Q1946+7658. The value for α corresponds to the redshift interval $2 < z < 3$.

Model	ω	s
Q0014+813		
CHDM	0.08	0.6263
ΛCDM_L	0.03	2.2
ΛCDM_H	0.05	0.90
tCDM	0.08	0.60
Q0302–003		
CHDM	0.075	0.74
ΛCDM_L	0.03	2.7
ΛCDM_H	0.05	1.09
tCDM	0.08	0.72
Q0636+680		
CHDM	0.075	0.82
ΛCDM_L	0.026	2.90
ΛCDM_H	0.045	1.15
tCDM	0.08	0.80
Q0956+122		
CHDM	0.06	0.54
ΛCDM_L	0.025	1.88
ΛCDM_H	0.045	0.81
tCDM	0.08	0.57
J2233–606		
CHDM	0.06	1.3
ΛCDM_L	0.024	4.5
ΛCDM_H	0.04	1.95
tCDM	0.06	1.25

Table 5. Continuum offsets and rescaling coefficients for the predicted distributions of optical depth per pixel to match those measured in Q0014+813, Q0302–003, Q0636+680, Q0956+122, and J2233–606.

QSO	flux ^a	wavelets ^b	N_{HI}^c	b ^c
Q1937–1009	ΛCDM_L	ΛCDM_H	all	tCDM
Q1946+7658	ΛCDM	ΛCDM_H	[all]	[CHDM]
Q0014+813	ΛCDM_L	CHDM	CHDM	none
Q0302–003	ΛCDM_L	CHDM	ΛCDM_L	none
Q0636+680	ΛCDM_L	tCDM	CHDM	tCDM
Q0956+122	ΛCDM_L	tCDM	CHDM	CHDM
J2233–606	none	CHDM	[all]	[CHDM]

Table 6. Summary of best-fitting model for each test and QSO.

^a Test based on the flux distribution per pixel. For Q1946+7658, the results are comparable for ΛCDM_L and ΛCDM_H .

^b Test based on velocity range containing measured median b -value.

^c Test based on AutoVP fits. When all fits correspond to $P_{\text{KS}} < 0.001$, ‘none’ is indicated. When all results are comparable (and $P_{\text{KS}} > 0.001$), ‘all’ is indicated. Bracketed results refer to basing the comparison only after removing lines with $b < 15 \text{ km s}^{-1}$ for Q1946+7658, or after removing identified metal lines from J2233–606.

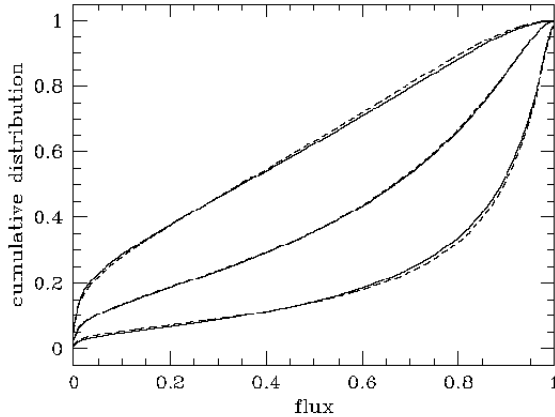


Figure A1. Test of the interpolation method for the flux distribution, for the Λ CDM_H model. The left pair of curves show the flux distribution at $z = 4$ (solid curve) and the predicted distribution based on rescaling the model spectra at $z = 3$ according to equation 1 (dashed curve). The right pair of curves show the flux distribution at $z = 3$ (solid curve) and the predicted distribution from rescaling the spectra at $z = 4$ (dashed curve). The central pair show the flux distribution at $z = 3.6$ (solid curve) and the linearly interpolated distribution based on rescaling the spectra at $z = 3$ and $z = 4$ and using equation 2 (dashed curve). The predicted and actual distributions at $z = 3.6$ agree to within 0.4%.

APPENDIX A: TESTS OF ANALYSIS PROCEDURES

In this section we summarise several tests of the analysis procedures: the redshift interpolation method, the noise models, the goodness-of-fit of the absorption line analyses, and the applicability of the KS test.

A1 Redshift interpolation

We test the redshift interpolation method using the distributions found in the Λ CDM_H simulation. In Figure A1, the effect of rescaling the flux distributions at $z = 3$ and $z = 4$ to redshifts $z = 4$ and $z = 3$, respectively, is shown using the values for α in Table 3 and equation 1. (No additional evolution in the radiation field was assumed: $p = 0$.) The result of rescaling the spectra at $z = 3$ and $z = 4$ both to $z = 3.6$ and then linearly weighting the resulting flux distributions to $z = 3.6$ using equation 2 is shown by the central dashed curve. The difference between the direct and inter-

polated cumulative distributions at $z = 3.6$ is at most 0.006, and indicates the level of accuracy of the modelling of the measured spectra. A similar level of accuracy is found for the cumulative distributions of the wavelet coefficients. The direct and interpolated distributions of the absorption line parameters, however, agree somewhat more poorly. While the cumulative distributions generally agree to within a difference of 0.01, portions may disagree by as much as 0.03 for the N_{HI} distribution and 0.04 for the b distribution at intermediate values, in the sense that the interpolated distributions exceed the directly estimated distributions. These differences are comparable to the accuracy to which the distributions may be measured using a single QSO spectrum and represent a limitation of the modelling of the distributions. Since it was based on a near maximum amount of interpolation to an intermediate redshift between the data dump redshifts, we expect that the actual modelling is somewhat better. Nonetheless, in the future a greater number of intermediate data dump redshifts would be desirable.

A2 Noise models

The differences in the two noise models described in §2.1, one based on a noise level independent of flux and one a function of the flux, have been tested using the predicted flux distribution and AutoVP analysis of the Λ CDM_L model for Q1937–1009, assuming no continuum offset. The difference between the measured and predicted cumulative flux distributions using a flux-independent noise level gives $d_{\text{KS}} = 0.0398$, while the flux-dependent noise level model prediction gives $d_{\text{KS}} = 0.0404$, essentially unchanged. The cumulative distributions for the N_{HI} and b distributions are nearly identical for both noise models, although there are small systematic shifts. The flux-independent noise model applied to the Λ CDM_L simulation gives for the cumulative N_{HI} distribution $d_{\text{KS}} = 0.067$ while the flux-dependent noise model gives $d_{\text{KS}} = 0.075$, resulting in a slightly poorer match. The flux-independent and flux-dependent noise models give for the cumulative b -distributions $d_{\text{KS}} = 0.10$ and $d_{\text{KS}} = 0.11$, respectively, again resulting in slightly poorer agreement. Although the resulting distributions show a slight sensitivity to the adopted noise model, the differences are small compared with those due to the uncertain continuum level, particularly on the b -distribution.

A3 Absorption line goodness-of-fit

Because of the necessarily automated nature of the absorption line parameter analyses, it is important to maintain a check on the acceptability of the fits. This was done by tabulating the distributions of χ^2 for the fit line complexes for all of the analyses. Because the number of degrees-of-freedom n_{dof} differs for different line complexes, the quantity tabulated is $(\chi^2/n_{\text{dof}} - 1)/(2/n_{\text{dof}})^{1/2}$, which in the limit $n_{\text{dof}} \rightarrow \infty$ is distributed like a gaussian with zero mean and unit variance (Kendall & Stuart 1969). The resulting cumulative distributions for the Λ CDM_L model predictions for Q1937–1009 (assuming no continuum offset) are shown for AutoVP and SPECFIT in Figure A2, which are representative of all the analyses. The fits are generally acceptable, although both line analysis methods produce a tail of high

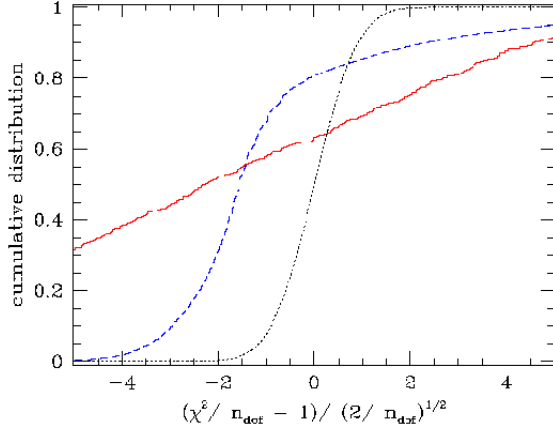


Figure A2. Distribution of χ^2 for the absorption line fits using AutoVP (solid curve) and SPECFIT (dashed curve), for Λ CDM_L. Shown are the cumulative distributions of $(\chi^2/n_{\text{dof}} - 1)/(2/n_{\text{dof}})^{1/2}$, where n_{dof} is the number of degrees-of-freedom of the fit. This quantity should be distributed like a gaussian with vanishing mean and unit variance in the limit $n_{\text{dof}} \rightarrow \infty$ (dotted curve). Although most of the fits are acceptable, both methods produce too great a tail at large χ^2 values.

χ^2 values. The low median value of χ^2 produced by AutoVP is a consequence of the demand for a reduced χ^2 of 0.5 for a fit to be acceptable. For SPECFIT, the requirement was a reduced χ^2 of 1.

A4 KS test

The acceptability of a hypothesis using the KS test is determined by the probability of exceeding the value $N^{1/2}d_{\text{KS}}$, where d_{KS} is the maximum difference (in absolute value) between the cumulative distribution of some parameter measured independently N times, and the predicted distribution. The probability distribution for exceeding $N^{1/2}d_{\text{KS}}$ derived from the simulated spectra of the Λ CDM_L model (with no continuum offset), using as the fiducial the average distribution of flux per pixel predicted for Q1937–1009, is shown in Figure A3. The distribution of $N^{1/2}d_{\text{KS}}$ derived from the simulated spectra is broader than the theoretical KS probability distribution. Also shown are the probability distributions of $N^{1/2}d_{\text{KS}}$ based on the distributions of N_{HI} and b from the AutoVP analysis. In contrast to the case for the flux, these distributions are much narrower than the theoretical distribution.

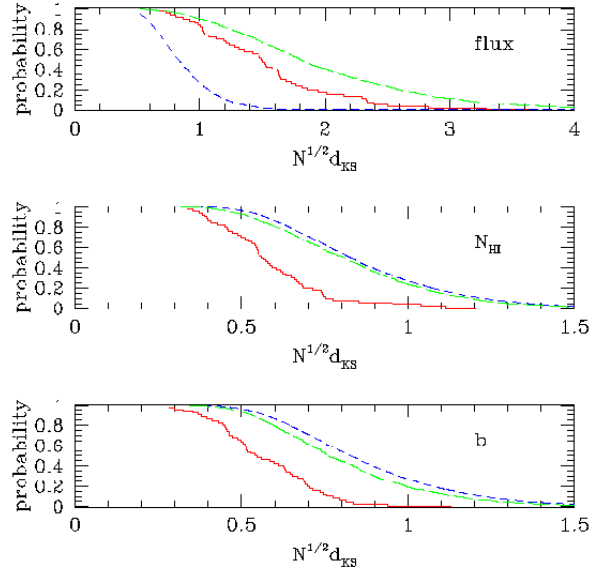


Figure A3. Test of the distribution of probability of exceeding a given value of $N^{1/2}d_{\text{KS}}$, where d_{KS} is the maximum difference between the cumulative distribution of N values of flux (top panel), N_{HI} (middle panel), and b (bottom panel), and the expected distributions, using the predictions of the Λ CDM_L model for Q1937–1009. The probability distribution derived from the simulation (solid curve) is broader for the flux, and narrower for the absorption line parameters, than the respective KS probability distributions (short dashed curve). The distributions for a set of Monte Carlo realisations of the Ly α forest are also shown (long dashed curves).

The reasons for the discrepancies in the distributions are unclear. Since absorption features typically run over several pixels, individual pixel fluxes will not be statistically independent, as is required for the validity of the KS test. Similarly, since the absorption line analysis procedure fits nearby lines simultaneously, the values found for the fit parameters are not truly independent.

We examine the possible effect of correlations in flux and in the derived absorption parameter values using a set of Monte Carlo simulations of spectra. We model the statistical distribution of the line positions, H I column densities, and Doppler parameters based on the distributions reported in Kirkman & Tytler (1997) (see Appendix B below). The resulting probability distribution of $N^{1/2}d_{\text{KS}}$ for the flux, shown in Figure A3, is again found to be broader than the KS distribution, and even broader than the distribution derived from the simulation. This suggests that strong correlations in the pixel fluxes are present. For the same level of rejection (same P_{KS}), a value for d_{KS} about a factor of 2 greater than predicted by the KS test is allowed. The re-

sulting probability distributions of $N^{1/2}d_{\text{KS}}$ based on the derived values of N_{HI} and b using AutoVP are found to be narrower than the KS distribution, although not by as much as the simulation results. Once again, correlations appear to be present, but tending to reduce the scatter in the derived values of the absorption line parameters.

An element of statistical dependence in the simulation results may also arise because the lines-of-sight sampled in the simulation are not truly stastically independent since they are drawn from the same simulation, and so may give a biased estimate of the correct distribution function. This may only be tested using lines-of-sight that are spaced adequately to probe separate structures, or by a large number of repeated simulations. Neither is currently computationally feasible using full hydrodynamical simulations, so that this possibility cannot be tested at present.

Still another possibility is that the properties of nearby features are physically related. Such correlations are expected for neighbouring lines-of-sight as a consequence of the linear continuity of the gas density defining the filaments. Similar correlations may exist among density fluctuations across the filaments. In this paper, we quote formal KS probabilities, noting that these appear to underestimate the true probabilities for the flux distribution comparisons and to be conservative estimates of the probabilities for the comparisons of the absorption line parameter values.

APPENDIX B: COMPARISON OF AutoVP AND SPECFIT

In this Appendix, the line finding and fitting algorithms used in this paper, AutoVP and SPECFIT, are compared using Monte Carlo realisations of spectra. The algorithm for AutoVP is described by Davé et al. (1997). SPECFIT performs its analysis through the following steps: 1. filter the spectrum using wavelets, discarding the smallest wavelet coefficients to ensure a reduced χ^2 of 1 between the filtered and unfiltered spectrum; 2. identify candidate features as inflection points by computing a smoothed second derivative of the spectrum; 3. define a spectral region to be fit about each candidate line as a contiguous region with the flux smaller than a given $\exp(-\tau_{\text{min}})$; 4. merge overlapping regions into single regions, provided the number of candidates in a single region is not too great, in which case it is split (at most 16 candidate lines were allowed in a single fit region in the analyses of this paper); 5. perform a non-linear least squares fit of the candidate lines to the original (unfiltered) spectrum.

The spectra are constructed from discrete lines with Voigt profiles using the H I column density and Doppler parameter distributions found by Kirkman & Tytler (1997). Specifically, the H I column densities N_{HI} are drawn independently from a power law distribution of slope 1.5 between $12.5 < \log_{10} N_{\text{HI}} < 16$ and the Doppler parameters b from a gaussian with mean 23 km s^{-1} and standard deviation 14 km s^{-1} . A cut-off in b is imposed according to $b > 14 + 4(\log_{10} N_{\text{HI}} - 12.5) \text{ km s}^{-1}$. The resulting average Doppler parameter is 31 km s^{-1} . The number density of lines per unit redshift matches that of Kirkman & Tytler (1997) at $z = 3$. The resolution is set at $\lambda/d\lambda = 5 \times 10^4$, and gaussian noise is added to give a continuum signal-to-noise ratio per pixel of 50.

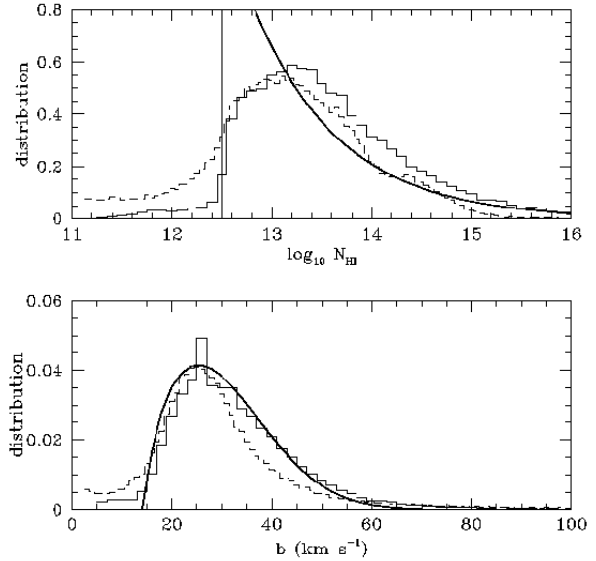


Figure B1. The recovered H I column density and Doppler parameter distributions from a set of Monte Carlo realizations. The light solid curves show the results of AutoVP while the dashed curves show the results of SPECFIT. The heavy solid lines show the input model distributions.

The two methods are found to have relative advantages and disadvantages. AutoVP faithfully recovers the cut-off in the H I column density distribution at $\log_{10} N_{\text{HI}} = 12.5$, while SPECFIT produces an excess of low column density systems. At higher column densities ($13 < \log_{10} N_{\text{HI}} < 15$), however, SPECFIT is found to better recover the input column density distribution.

By contrast, AutoVP well reproduces the input Doppler parameter distribution, although it produces a small tail at low values. SPECFIT similarly produces a low b tail, and somewhat underpredicts the number of intermediate b systems.

It is evident that neither algorithm perfectly recovers the input parameter distributions. No improvement in the signal-to-noise ratio would yield better results: the discrepancy arises from the unavoidable blending of features. In practice, provided the same algorithm is applied to the data and the model spectra, the resulting fits may still be used as a viable statistical description of the light fluctuations in the spectra.

REFERENCES

- Bardeen J. M., Bond J. R., Kaiser N., Szalay A. S., 1996, ApJ, 304, 15

- Bertschinger E., 1995, astro-ph/9506070
- Bond J. R., Wadsley J. W., 1997, in Petitjean P., Charlot S., eds, Structure and Evolution of the Intergalactic Medium from QSO Absorption Line Systems. Editions Frontières, Paris, p. 143
- Bryan G. L., Machacek M., Anninos P., Norman M. L., 1999, ApJ, 517, 13
- Bryan G. L., Machacek M. E., 2000, ApJ, 534, 57
- Bunn E. F., White M., 1997, ApJ, 480, 6
- Burles S., Tytler D., 1997, AJ, 114, 1330
- Burles S., Tytler D., 1998, ApJ, 499, 699
- Cen R., Miralda-Escudé J., Ostriker J. P., Rauch M., 1994, ApJ, 437, L9
- Cristiani S., D'Odorico V., 2000, AJ, 120, 1648
- Davé R., Hernquist L., Weinberg D. H., Katz N., 1997, ApJ, 477, 21
- de Bernardis P. et al., 2000, Nature, 404, 955
- Eisenstein D. J., Hu W., 1999, ApJ, 511, 5
- Fang Y., Crofts P. S., 1995, ApJ, 440, 69
- Giallongo E., Cristiani S., Trevese T., 1992, ApJ, 398, L9
- Haardt F., Madau P., 1996, ApJ, 461, 20
- Hernquist L., Katz N., Weinberg D., Miralda-Escudé J., 1996, ApJ, 457, L51
- Hu E. M., Kim T. S., Cowie L. L., Songaila A., Rauch M., 1995, AJ, 110, 1526
- Hui L., Rutledge R. E., 1999, ApJ, 517, 541
- Kendall M. G., Stuart A., 1969, The Advanced Theory of Statistics, vol. 1, Charles Griffin & Co., London
- Kirkman D., Tytler D., 1997, ApJ, 484, 672
- Machacek M. E., Bryan G. L., Meiksin A., Anninos P., Thayer D., Norman M. L., Zhang Y., 2000, ApJ, 532, 118 (M00)
- Meiksin A., 1994, ApJ, 431, 109
- Meiksin A., Madau P., 1993, ApJ, 412, 34
- Meiksin A., White M., 2000, astro-ph/0008214
- Meiksin A., 2000, MN, 314, 566
- Rauch M. et al., 1997, ApJ, 489, 7
- Seljak U., Zaldarriaga M., 1996, ApJ, 469, 437
- Steidel C. C., Adelberger K. L., Giavalisco M., Dickinson M., Pettini M., 1999, ApJ, 519, 1
- Steidel C. C., Sargent W. L. W., 1987, ApJ, 318, L11
- Theuns T., Leonard A., Efstathiou G., 1998, MNRAS, 297, L49
- Webb J. K., Barcons X., Carswell R. F., Parnell H. C., 1992, MNRAS, 255, 319
- Zhang Y., Anninos P., Norman M. L., 1995, ApJ, 453, L57
- Zhang Y., Anninos P., Norman M. L., Meiksin A., 1997, ApJ, 485, 496
- Zhang Y., Meiksin A., Anninos P., Norman M. L., 1998, ApJ, 495, 63